Deformation Correction in Ultrasound Imaging in an Elastography Framework

MASSACHUSETTS INSTITUTE OF TECHNOLOGY
JAN 04 2011
LIBRARIES

ARCHIVES

by

Shih-Yu Sun
B.S. Electrical Engineering, National Taiwan University (2006)

Submitted to the Department of Electrical Engineering and Computer Science
in partial fulfillment of the requirements for the degree of

Master of Science in Electrical Engineering and Computer Science

at the

MASSACHUSETTS INSTITUTE OF TECHNOLOGY

September 2010

© Massachusetts Institute of Technology 2010. All rights reserved.

Author....................................
Department of Electrical Engineering and Computer Science
August 27, 2010

Certified by...
Brian W. Anthony
Research Scientist, Department of Mechanical Engineering
Thesis Supervisor

Accepted by...
Terry P. Orlando
Chair, Department Committee on Graduate Students

Deformation Correction in Ultrasound Imaging in an Elastography Framework

by

Shih-Yu Sun

Submitted to the Department of Electrical Engineering and Computer Science
on August 27, 2010, in partial fulfillment of the
requirements for the degree of
Master of Science in Electrical Engineering and Computer Science

Abstract

Tissue deformation in ultrasound imaging is an inevitable phenomenon and poses challenges to the development of many techniques related to ultrasound image registration, including multimodal image fusion, freehand three-dimensional ultrasound, and quantitative measurement of tissue geometry. In this thesis, a novel trajectory-based method to correct tissue deformation in ultrasound B-mode imaging and elastography is developed in the framework of elastography.

To characterize the change of tissue deformation with contact force, a force sensor is used to provide contact force measurement. Correlation-based displacement estimation techniques are applied to ultrasound images acquired under different contact forces. Based on the estimation results, a two-dimensional trajectory field is constructed, where pixel coordinates in each scan are plotted against the corresponding contact force. Interpolation or extrapolation by polynomial curve fitting is then applied to each trajectory to estimate the image under a specified contact force.

The performance of displacement estimation and polynomial curve fitting are analyzed in a simulation framework incorporating FEM and ultrasound simulation. Influences of parameter selection are also examined. It is found that in displacement estimation, the coarse-to-fine approach outperforms single-level template search, and correlation filtering in coarse scale provides noticeable improvement in estimation performance. The strategies of image acquisition and order selection in polynomial curve fitting are also evaluated. Additionally, a finer force resolution is found to give better performance in predicting pixel positions under zero force.

Deformation correction in both B-mode imaging and elastography is demonstrated through simulation and *in-vitro* experiments. The performance of correction is quantified by translational offset and area estimation of the tissue inclusions. It is found that, for both B-mode and elastography images, those performance metrics are significantly improved after correction. Moreover, it is shown that a finer resolution in force control gives better performance in deformation correction, which agrees with the analysis of polynomial curve fitting.

Thesis Supervisor: Brian W. Anthony
Title: Research Scientist, Department of Mechanical Engineering

Acknowledgements

I would like to thank my advisor, Dr. Brian Anthony, for his guidance. Brian always gives inspiring advices in conducting the research and shows great patience during discussion. I learn a lot more than doing research from working with him.

I would also like to thank Matthew Gilbertson. His awesome probe system has enabled me to test various ideas and validate the proposed method. I am often amazed by Matthew's skills in mechanical design and machining. I believe he can make anything with a block of metal.

Last but not least, I would like to thank my parents Kao-Chin Sun and Shu-Huei Chen, my sisters Yi-Chun and Yu-Ting for being extremely supportive to me. And thank you, Yi-Ping. Your unconditional friendship, company, and love have been, and will always be, invaluable to my life.

Contents

1 **Introduction** 15

1.1 Related Work 16
1.2 Contributions 17
1.3 Thesis Outline 17

2 **Background** 19

2.1 Ultrasound B-mode Imaging 19
2.2 Ultrasound Elastography 20
2.3 Summary 24

3 **Trajectory-Based Deformation Estimation and Correction** 25

3.1 Concept 25
3.2 Two-Dimensional Displacement Estimation 27
  3.2.1 Correlation-Based Template Matching 28
  3.2.2 Coarse-to-Fine Search 30
  3.2.3 Correlation Filtering 30
  3.2.4 Subsample Estimation 33
  3.2.5 Smoothing with Non-Uniform Spatial Resolution 35
3.3 Polynomial Curve Fitting 37
3.4 Summary 37

4 **Ultrasound Simulation Using Finite-Element Methods** 39

4.1 Simulation Setup 39
  4.1.1 FEM 39
  4.1.2 Field II 41
4.2 Displacement Estimation 42
  4.2.1 Single-Level and Coarse-to-Fine Search 42
  4.2.2 Analysis of Parameter Selection 47
4.3 Curve Fitting 50

4.3.1 Noise Modeling in Displacement Estimation 51
4.3.2 Analysis of Parameter Selection 53
4.4 Deformation Estimation and Correction 55
4.4.1 Deformation Correction with 100mN Force Resolution 56
4.4.2 Comparison of Force Resolutions 60
4.5 Summary 62

5 *In-Vitro* Experiments 65
5.1 Experiment Setup 65
5.1.1 Force-Controlled Ultrasound Probe 66
5.1.2 Ultrasound Imaging System 68
5.2 Experiment Results and Discussion 69
5.3 Summary 72

6 Conclusions 73
6.1 Summary 73
6.2 Future Work 74

Bibliography 77

List of Figures

1-1 The ultrasound images of brachial artery under varying levels of probe compression 15

2-1 Only envelopes of the reflected signal are used for B-mode image formation, but additional information about the phase is inherent in the RF data. 20

2-2 Illustration of strain estimation: in (a), a definition of strain is given; in (b), the same concept is applied on a displacement field. 22

2-3 The simulated pre-compression and post-compression B-mode images. ...23

2-4 The displacement estimation results (a) and the corresponding strain image (b) in the simulated ultrasound elastography 23

3-1 The B-mode image of a homogeneous tissue under compression and the corresponding displacement field 26

3-2 Behaviors of tissue deformation under varying contact forces could be characterized by tracking pixel movements along the ultrasound image sequence 26

3-3 The image under a specified contact force could be estimated from the trajectory field, which describes pixel movement with changing contact forces. 27

3-4 An overview of the 2D displacement estimation method 28

3-5 Displacement estimation is performed based on a template-matching scheme using the waveforms inherent in the ultrasound images 29

3-6 Illustration of the correlation filtering method. 31

3-7 Illustration of coarse-scale displacement estimation 32

3-8 Design of the fine-scale search region to reduce possible peak detection errors brought by correlation filtering 33

3-9 Curve fitting using three sample points is applied in two directions for subsample accuracy in displacement estimation 34

3-10 (a) simulated axial displacement estimation results; (b) the black dots

indicate the occurrence of peak-hopping errors in the estimation results ...36
3-11 (a) computed correlation coefficients in axial displacement estimation; (b) the black dots indicate the locations where the correlation coefficients are lower than 0.5 36

4-1 The setup in FEM 40
4-2 A sampled set of the scatterers in ultrasound simulation 42
4-3 The axial displacement estimation MAE (a) and peak-hopping errors (b) versus the applied strain 45
4-4 The axial displacement estimation MAE (a) and peak-hopping errors (b) versus the probe elevational offset 45
4-5 The axial displacement estimation MAE (a) and peak-hopping errors (b) versus SNR 46
4-6 The lateral displacement estimation MAE versus the strain (a), elevational offset (b), and SNR (c) 47
4-7 The axial displacement estimation MAE (a) and peak-hopping errors (b) versus the coarse-scale kernel length 48
4-8 The axial displacement estimation MAE (a) and peak-hopping errors (b) versus the fine-scale kernel length 49
4-9 The axial displacement estimation MAE (a) and peak-hopping errors (b) versus the coarse-scale correlation filter length 50
4-10 The lateral displacement estimation MAE versus the coarse-scale kernel length (a), the fine-scale kernel length (b), and the coarse-scale filter length (c) 50
4-11 Selected strain-force points for varying force resolutions: 20mN, 50mN, and 100mN 52
4-12 Illustration of displacement error induced by noise in force control 53
4-13 Projection MAE versus the polynomial order: eight frames with a 100mN resolution 54
4-14 Projection performance versus the number of frames used for varying force resolutions 55
4-15 The B-mode image of the 300 mN-compressed inclusion (a) is corrected (b). From the comparison between (a), (b) and the true

uncompressed inclusion contour (c), it is shown that the deviation in the position of the inclusion can be remedied. (d) 57

4-16 The performance of deformation correction is quantified by three parameters that are derived from area estimation. They are true positive (TP), false positive (FP), and false negative (FN). 58

4-17 The elastography image under 200-300 mN compression (a) is corrected (b). From the comparison between (a), (b) and the true uncompressed inclusion contour (c), it is shown that the deviation in the position of the inclusion can be remedied. (d) 59

4-18 Deformation correction of B-mode images: compare 20 mN, 50 mN, and 100 mN force resolution 60

4-19 Difference images between the corrected B-mode images and the true uncompressed image using 20 mN, 50 mN, and 100 mN force resolution 61

4-20 Deformation correction of elastography: compare 20 mN, 50 mN, and 100 mN force resolution 62

5-1 The breast ultrasound needle biopsy phantom used in the *in-vitro* experiment (from http://www.cirsinc.com/) 65

5-2 The *in-vitro* experiment setup 66

5-3 The force-controlled ultrasound probe 67

5-4 GUI of the force-controlled probe 67

5-5 GUI of the ultrasound imaging system 68

5-6 The B-mode image of the 4 N-compressed inclusion (a) is corrected to 1 N compression (b). From the comparison between (a), (b) and the true 1 N-compressed inclusion contour (c), it is shown that the deviation in the shape and position of the inclusion can be remedied. (d) 70

5-7 The elastography image under 3.5-4 N compression (a) is corrected to 1 N compression (b). From the comparison between (a), (b) and the true 1 N-compressed inclusion contour (c), it is shown that the deviation in the position of the inclusion can be remedied. (d) 71

List of Tables

4-1 The hyperelastic parameters of normal and pathological breast tissue in FEM 41
4-2 Parameters for the search schemes 43
4-3 The efficient orders for each pair of force resolution and number of frames 54
4-4 The most efficient number of frames and the corresponding efficient order for each force resolution 55
4-5 Performance of correcting the B-mode image contour under 300 mN compression as measured by the translational offset from the true uncompressed contour and the area estimation parameters 58
4-6 Performance of correcting the elastography image contour under 200-300 mN compression as measured by the translational offset from the true uncompressed contour and the area estimation parameters 59
4-7 Performance of correcting the B-mode image contour under 100mN compression using 20 mN, 50 mN, and 100 mN force resolution as measured by the translational offset from the true uncompressed contour and the area estimation parameters 61
4-8 Performance of correcting the elastography image contour under 100-(120 mN, 150 mN, 200 mN) compression using 20 mN, 50 mN, and 100 mN force resolution as measured by the translational offset from the true uncompressed B-mode image contour and the area estimation parameters 62

5-1 Performance of correcting the 4 N-compressed B-mode image contour to 1 N compression as measured by the translational offset from the true 1 N-compressed contour and the area estimation parameters 70
5-2 Performance of correcting the elastography image contour under 3.5-4 N compression to 1 N compression as measured by the translational offset from the true 1 N-compressed B-mode image contour and the area estimation parameters 71

Chapter 1

Introduction

Diagnostic ultrasound imaging technology is indispensable nowadays as it provides inexpensive and non-invasive real-time imaging with high spatial resolution. Ultrasound imaging is typically performed in a manner where a probe makes firm contact with the skin for good image quality. In this procedure, deformation of the underlying tissue is inevitable, and thus structures shown in imaging are distorted. This phenomenon is shown in Figure 1-1, where the appearance of the same tissue changes due to varying levels of probe compression. The blob of tissue enclosed by dashed lines undergoes translational offset, and the cross-sectional area of the brachial artery (enclosed by solid lines) shrinks with an increased compression level.

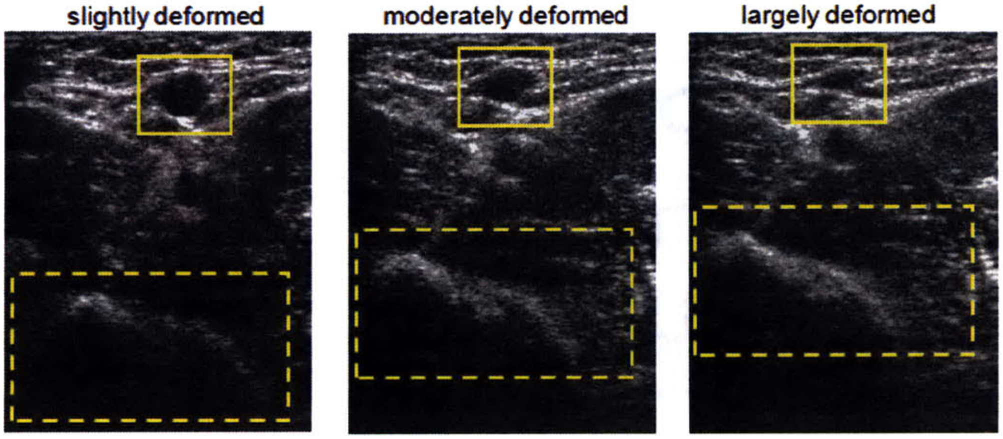

Figure 1-1 The ultrasound images of brachial artery under varying levels of probe compression

In most cases, this distortion effect does not impede diagnosis, since most of the characteristics of tissue are retained under compression. In fact, tracking pixel displacements in a sequence of compressed tissue images provides information to discriminate between normal and pathological tissue in elastography. [1] However, for applications where the undeformed appearance of biological tissue is required, avoiding or correcting tissue deformation becomes crucial. For example, in freehand three-dimensional ultrasound (freehand 3D US), where the shape of tissue is reconstructed by stacking two-dimensional (2D) slices acquired in varying probe positions and contact forces, the corresponding pixels can be accurately aligned only if the deformation patterns in each slice can be appropriately corrected. Furthermore, deformation correction applied in 3D US facilitates quantitative measurement of tissue volumes and analysis of the shape. [2] The need to correct deformation also arises in multimodal image processing, in which tissue deformation in ultrasound scanning has to be corrected before the image can be accurately registered with those from other imaging modalities, such as X-ray, optical coherence tomography (OCT), computed tomography (CT), and magnetic resonance imaging (MRI). Other applications that could potentially benefit from the deformation correction method include computational anatomy and image-guided surgery [3],[4].

1.1 Related Work

Several deformation correction methods have been proposed, aiming to estimate B-mode images that would have been acquired in ultrasound scanning as if there had been no probe contact. In the surface model method proposed by Burcher *et al.* [2], the compression level of each scan frame are estimated using probe contact force measurement. Inter-frame registration is achieved, but this method does not address in-plane deformation of the underlying tissue. In [5], Treece *et al.* proposed a method that is able to correct in-plane deformation along the axial direction, which is the most significant effect due to probe compression. This method estimates tissue deformation by combining probe position measurement and image-based registration. However, the method becomes inadequate when it is important to characterize tissue deformation in two or three dimensions. Also, in this method, tissue elasticity is assumed to be uniform over the whole region of interest, but it is rarely the case in biological tissue.

A method that takes into account two-dimensional pixel movement was proposed by Burcher *et al.* [2], where tissue deformation patterns are predicted based on contact force measurement and finite-element modeling. Correction of deformation is performed by an inverse approach. Nevertheless, this method incorporates *a priori* knowledge of the spatial variation of tissue elasticity, which can be hard to measure in clinical settings.

To reduce dependence on assumptions of tissue elastic property, a preliminary study of trajectory-based deformation correction is described in the work of Burcher [6]. In this method, pixel trajectories under varying compression levels are estimated by B-mode speckle tracking. [7] Linear polynomial functions are then used to fit the trajectories to predict tissue geometry under a specified compression level. Encouraging *in-vivo* results of inclusion contour prediction are presented. However, this method models the mechanical behaviors of biological tissue deformation by linear dynamics. This approximation is applicable only when the range of applied contact forces is small.

1.2 Contributions

In this thesis, a novel deformation correction method developed within the framework of ultrasound elastography is described. This method allows integration with the existing elastography technique and requires no additional operator effort in the workflow. The contributions include:

- A novel application of elastography to solve the deformation correction problem in ultrasound imaging.
- The ability of this method to correct tissue deformation when the range of applied contact forces is large
- Extension of deformation correction methods to addressing tissue deformation in ultrasound elastography
- An ultrasound simulation platform incorporating FEM and Field II for the verification of algorithms involving imaging of biological tissue in varying compression states

1.3 Thesis Outline

The remainder of this thesis is organized as follows. In Chapter 2, current technologies in ultrasound imaging are briefly introduced, including B-mode imaging and elastography. Chapter 3 describes the concept of the proposed trajectory-based deformation correction method and details of the algorithm. This method is validated by simulation and *in-vitro* experiments, which are presented in Chapter 4 and Chapter 5, respectively. This thesis concludes in Chapter 6 with a summary of the above chapters and a discussion of future work for possible improvement and extension of the proposed method.

Chapter 2

Background

The deformation correction method proposed in this thesis is developed within the framework of ultrasound elastography and is applicable to both ultrasound B-mode images and elastography. This chapter provides an introduction to the existing technologies related to this method. Section 2.1 describes the physics and process of B-mode image formation. Section 2.2 presents the method to perform ultrasound elastography using probe compression.

2.1 Ultrasound B-mode Imaging

Ultrasound imaging is an indispensable diagnosis tool due to its low cost and real-time nature, and has been under active development for decades. This technology uses mechanical waves modulated by a carrier frequency of higher than 20kHz to interrogate the structures of the underlying tissue. The wave is generated from electrical excitation of a piezoelectric transducer and propagates through the human body via a layer of transmission gel. The transmitted wave is reflected in human body when interfaces of mismatched acoustic impedance are encountered. Therefore, the reflected waveform is determined by the spatial variation in acoustic impedance of tissue and sensed by the same transducer. Envelope detection is then performed on the received radio-frequency (RF) wave, as illustrated in Figure 2-1. After repeating this procedure at preprogrammed positions, the acquired envelopes are post-processed and aligned to form a brightness image, or B-mode image, that describes the tissue structure. Examples of B-mode images can be seen in Figure 1-1.

Conventionally, three specific terminologies are used to refer to the directions in ultrasound scanning; they are axial, lateral, and elevational directions. Axial and lateral directions refer to the two dimensions that define the scan plane, with axial direction being parallel to ultrasound beam propagation. Elevational direction is orthogonal to the scan plane.

It should be emphasized that although only envelopes of the reflected waves are used to form a B-mode image, the raw RF data provide additional information about the phase of wave propagation, which is often useful for purposes other than image formation. In Chapter 3, both the use of RF data and the envelopes for pixel displacement estimation are discussed. The performances are analyzed in Chapter 4.

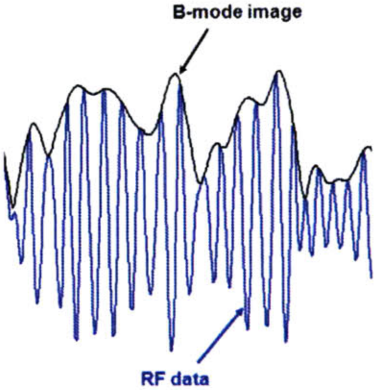

Figure 2-1 Only envelopes of the reflected signal are used for B-mode image formation, but additional information about the phase is inherent in the RF data.

2.2 Ultrasound Elastography

Spatial variation of brightness in B-mode images can describe the structure of tissue under the assumption that the acoustic impedance varies noticeably in different types of tissue. However, this assumption does not always hold. There are times when pathological tissue is not discernible from the surroundings in B-mode images. As a result, imaging methods that can detect tissue properties other than acoustic impedance are often desired.

Palpation has long been an effective method for diagnosis of pathologies. It is based on the fact that pathological tissue normally has higher stiffness than the surroundings. This observation implies that the ability to detect spatial variation in tissue stiffness could potentially assist diagnosis. One of the most popular methods for detecting this variation involves exerting a sequence of compression with an ultrasound probe on the tissue, imitating the practice of palpation, and acquiring images at the same time. Stiffness at each point of the tissue is then differentiated by tracking pixel displacements in the acquired images.

In solid mechanics, stiffness is often characterized by Young's modulus, which is defined as the ratio between stress and the induced strain at a particular point. Normally, to detect tissue abnormality in ultrasound images, strain is estimated instead of the Young's modulus. This simplification is based on the assumption that the stress field is uniform over the region of interest.

The definition and estimation of strain in elastography are illustrated in Figure 2-2. Suppose a rod with length L is squeezed by ΔL under a certain compression, as shown in Figure 2-2(a). The induced strain e is defined as

$$e = \frac{\Delta L}{L} \tag{2.1}$$

The same concept can be applied to estimating strain from the displacement field in Figure 2-2(b). It can be imagined that, when there is no compression, a tiny rod with length ε lies between (x_0, y_0) and $(x_0, y_0 + \varepsilon)$, where ε is the distance between neighboring pixels. Under the compression, the spatial distribution of displacements in y (the axial direction), $v(x, y)$, can be measured. Note that since the tissue is seen with respect to the coordinate system attached to the probe, points of the tissue in the image appear to be moving upward during compression.

Under the compression, the strain in y at the position (x_0, y_0), $e_y(x_0, y_0)$, can be approximated as $v(x_0, y_0) - v(x_0, y_0 + \varepsilon)$, the change in length of the rod, divided by the original length ε. Note that to observe only the variation in strain instead of the exact values, the division by ε can be omitted since it is a constant over the field. Therefore, in the implementation of strain imaging, only the term $v(x_0, y_0) - v(x_0, y_0 + \varepsilon)$ is used as the strain estimator for the given point (x_0, y_0).

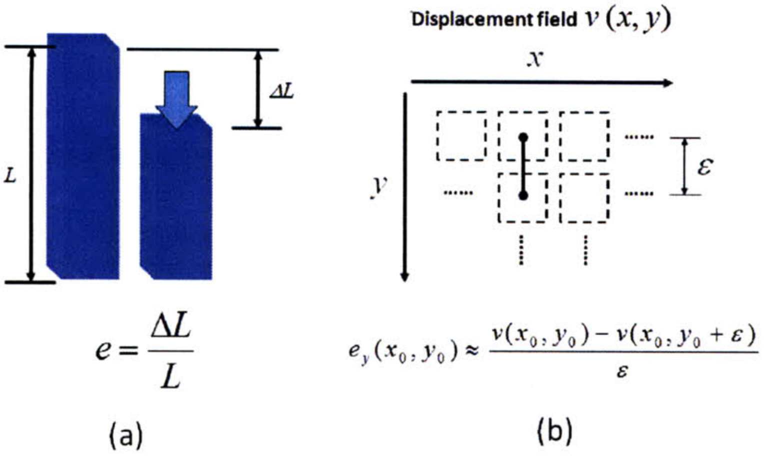
Displacement field $v(x,y)$
x
y
L
ΔL
ε
$e = \frac{\Delta L}{L}$
$e_y(x_0, y_0) \approx \frac{v(x_0, y_0) - v(x_0, y_0 + \varepsilon)}{\varepsilon}$
(a)
(b)

Figure 2-2 Illustration of strain estimation: in (a), a definition of strain is given; in (b), the same concept is applied on a displacement field.

It should be emphasized that, in ultrasound image formation, the spatial sampling distance in the axial direction is determined by the temporal frequency with which reflected ultrasound waves are sampled, whereas the sampling distance in the lateral direction is determined by the element width of the probe array. Therefore, the spatial resolution in the axial direction is much higher than that in the lateral direction. For the configuration of the Terason t3000 imaging system, for instance, the spatial sampling distance is about 26 μm axially and 150 μm laterally. [8] As a result, strain estimation is normally applied only in the axial direction for elastography, although the performance could be improved by incorporating estimation of lateral strain. [9]

In the following, a simulated example of ultrasound elastography is described to demonstrate the feasibility of detecting pathological tissue in elastography even if it is invisible in B-mode images (see Chapter 4 for the simulation framework.) A pre-compression and a post-compression B-mode image of a tissue phantom are shown in Figure 2-3. The elasticity in a circular region of the phantom is set to be higher than the surroundings to mimic pathological tissue, but the spatial distribution of acoustic impedance is set to be uniform over the whole field. As a result, the simulated pathological tissue region is not observable in the B-mode images.

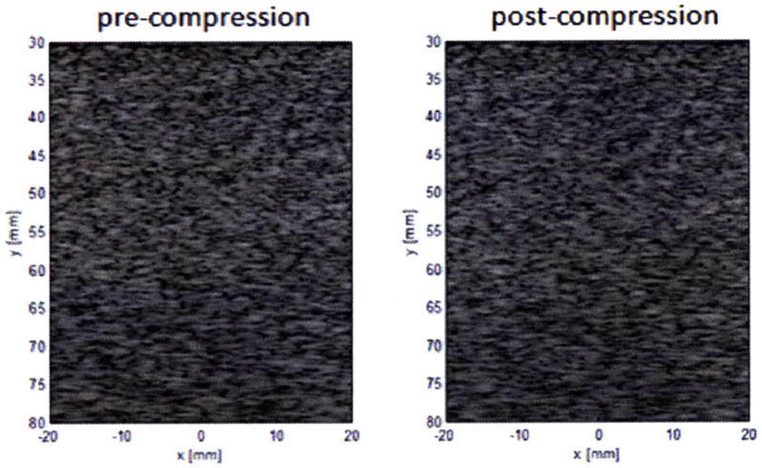
pre-compression
post-compression
y [mm]
x [mm]
30
35
40
45
50
55
60
65
70
75
80
-20
-10
0
10
20

Figure 2-3 The simulated pre-compression and post-compression B-mode images.

The results of displacement estimation in *y* are shown in Figure 2-4 (a) (see Chapter 3 for the displacement estimation algorithm.) By applying the strain estimator on the displacement field, the strain image is acquired as in Figure 2-4 (b). In the strain image, it is obvious that there is a nearly circular inclusion with less strain, which implies higher stiffness in the region under the assumption of uniform stress. This observation agrees with the simulation setup of tissue elasticity properties.

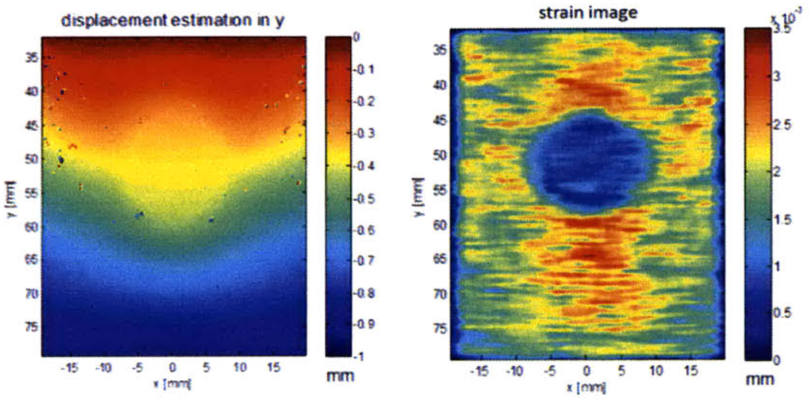

(a) (b)

Figure 2-4 The displacement estimation results (a) and the corresponding strain image (b) in the simulated ultrasound elastography

2.3 Summary

This chapter provided a brief introduction to ultrasound B-mode imaging and elastography. B-mode images are formed by aligning the envelopes of the received RF data. Estimation of the displacement field due to probe compression can be performed on either the RF data or the envelopes. Elastography is performed in the form of strain imaging using the displacement estimates. Through simulation, it has been shown that elastography can show pathological tissue even when it is invisible in B-mode imaging.

Chapter 3

Trajectory-Based Deformation Estimation and Correction

In this thesis, the trajectory-based deformation estimation and correction method is proposed to estimate the ultrasound B-mode and elastography images under a specified compression level, in which zero compression is of particular interest. The method involves modeling tissue deformation using pixel displacement fields and performing extrapolation or interpolation in the fields. In this chapter, this procedure is described in detail. Section 3.1 presents the high-level concept of the method. Section 3.2 covers the design of a two-dimensional displacement estimation algorithm. Section 3.3 describes the application of polynomial curve fitting to the estimated displacement fields to perform extrapolation.

3.1 Concept

The trajectory-based deformation estimation and correction method is an extension to the elastography technique. As described in Section 2.2, elastography uses a sequence of compressed tissue images and the corresponding displacement estimates to differentiate elasticity of the underlying tissue. Actually, these displacement estimates could also be used to model tissue deformation between the compression states. Figure 3-1 gives an example of the displacement field of a homogeneous tissue under compression.

To characterize the force-varying deformation patterns of the biological tissue under investigation, a sequence of ultrasound images under different contact forces are acquired, and the corresponding forces are measured by a force sensor installed in the probe. A set of displacement fields is established by tracking each pixel over the whole field of view along the image sequence, as shown in Figure 3-2. Here tissue deformation in the elevational direction is assumed to be negligible and is ignored in displacement estimation.

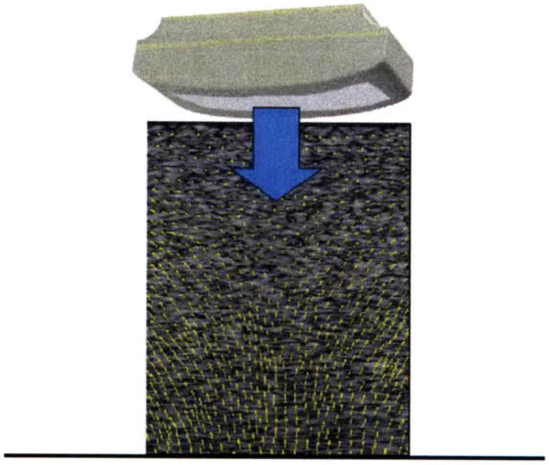

Figure 3-1 The B-mode image of a homogeneous tissue under compression and the corresponding displacement field

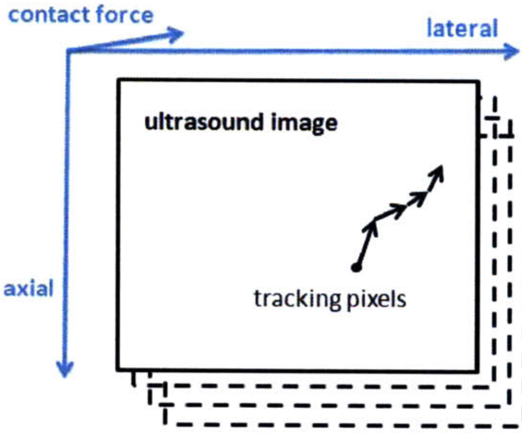

Figure 3-2 Behaviors of tissue deformation under varying contact forces could be characterized by tracking pixel movements along the ultrasound image sequence

Knowledge of contact forces and the pixel displacement fields allow the construction of a trajectory field for the specific subject, in which pixel coordinates in the scan planes are plotted against the corresponding contact forces, as shown in Figure 3-3. Pixel positions under a specified contact force are then estimated from the trajectories. Specifically, the locations of pixels under a specified contact force within the acquired force range could be estimated from linear interpolation between two neighboring forces. The images under contact forces beyond the acquired force range could be estimated by extrapolation. One selection of particular interest is zero force, which provides an estimate of the image that would have been acquired if there had been no contact force.

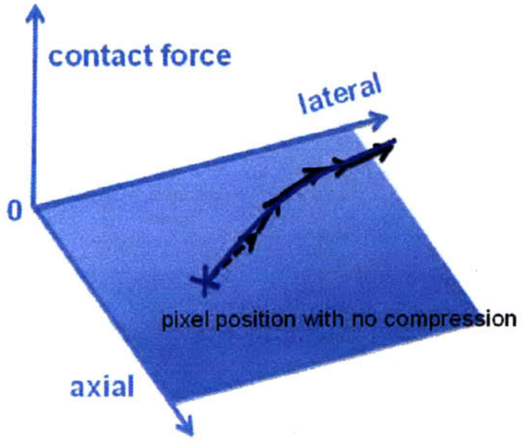

Figure 3-3 The image under a specified contact force could be estimated from the trajectory field, which describes pixel movement with changing contact forces.

3.2 Two-Dimensional Displacement Estimation

Displacement estimation is crucial in characterizing the force-varying tissue deformation patterns and is pivotal to the performance of the deformation correction method. Several methods have been developed to estimate pixel displacements in ultrasound images in both the axial and lateral direction, including B-mode block-matching [7],[10], phase-based estimation [11], RF speckle tracking [9],[12-15], and incompressibility-based methods [16],[17]. Those methods all pose displacement estimation as a time-delay problem, which has been extensively studied in the literature. [18]

In this thesis, a 2D displacement estimation algorithm is developed based on an iterative 1D displacement estimation scheme, where lateral displacement estimation is performed at the locations previously found in the corresponding axial estimation. [19] Coarse-to-fine template-matching is performed axially, with normalized correlation coefficients as a similarity measure. Subsample estimation accuracy is achieved by curve fitting. [20] This estimation algorithm is summarized in Figure 3-4, and the essential steps are detailed in the following subsections.

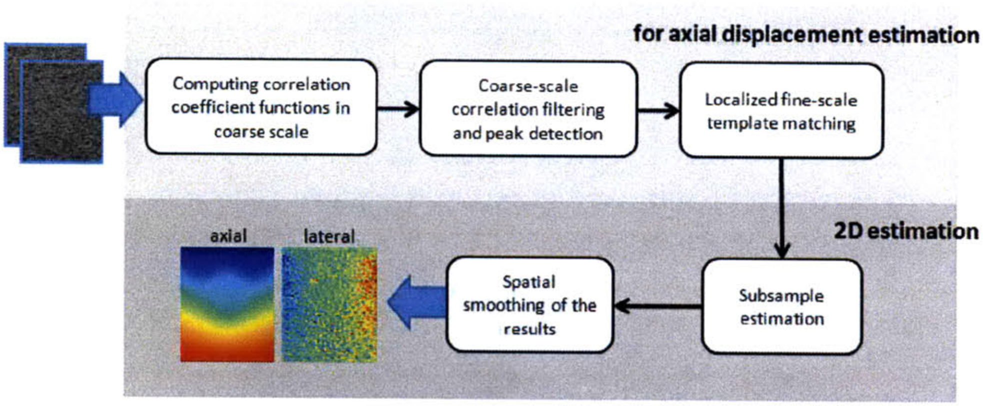
for axial displacement estimation
Computing correlation coefficient functions in coarse scale
Coarse-scale correlation filtering and peak detection
Localized fine-scale template matching
2D estimation
axial
lateral
Spatial smoothing of the results
Subsample estimation

Figure 3-4 An overview of the 2D displacement estimation method

3.2.1 Correlation-Based Template Matching

Template matching is one of the most frequently used methods in motion estimation. Figure 3-5 gives an example to illustrate the matching method in the axial direction, in which the displacement field is to be estimated between pre-compression (A) and post-compression (B) states. Suppose in image A, displacement of the location indicated by the orange dot is to be measured. A kernel centered at that point is defined to include the pre-compression segment $s_A(t)$, which is to be searched in image B. The search starts from the corresponding location in image B and moves along the post-compression waveform $s_B(t)$ to find the best match of the pre-compression segment. In a similar manner, all of the waveforms in image A are axially divided into overlapping kernels, and each of the segments is compared with the corresponding waveforms in image B.

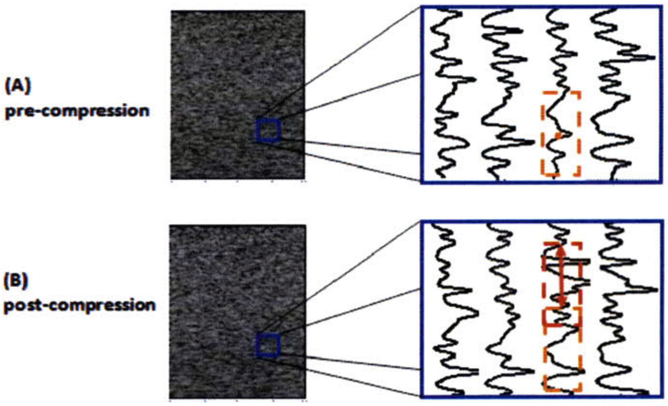

Figure 3-5 Displacement estimation is performed based on a template-matching scheme using the waveforms inherent in the ultrasound images

Among other frequently used similarity measures like MAE (Mean Absolute Error) and MSE (Mean Squared Error), the normalized cross correlation coefficient function $\rho(t, t+\tau)$ is used here, which is defined by

$$\rho(t, t+\tau) = \frac{\int_{\tau}^{\tau+T} (s_A(\varphi-\tau)-\mu_A)(s_B(\varphi)-\mu_B)d\varphi}{\sigma_A\sigma_B}, \tag{3.1}$$

where t denotes the point of estimation in the axial direction and τ denotes the lag of the correlation coefficient function. Here T denotes the time span of the correlation kernel. μ_A and μ_B are the mean values of $s_A(t)$ and $s_B(t)$, respectively. σ_A and σ_B are the standard deviations. After $\rho(t, t+\tau)$ is estimated, peak detection is performed on this function. The lag that gives the peak is considered the location corresponding to the best match. Note that only the sampled version of $\rho(t, t+\tau)$ is acquired, so interpolation is performed to find the peak of $\rho(t, t+\tau)$ and the corresponding lag. (See Section 3.2.4 for the interpolation method)

Note that here displacement estimation in tissue compression is approximated as a time-delay problem, in which there is assumed to be no intra-kernel deformation. However, when the chosen kernel length T is relatively large under the applied strain, this approximation error becomes noticeable, and as a result, the location of correlation peak might deviate from the true displacement value. On the other hand, increasing the number of samples in correlation estimation could reduce the variance of estimation error. Therefore, in determining the kernel length *T*, one should consider the tradeoff between minimization of the mean and the variance of correlation estimation error.

In addition to estimation accuracy, the dynamic range of the algorithm should also fulfill the need of the specific application. The range is significantly influenced by the search length in template matching, which is equivalent to the length of the estimated correlation coefficient function. Although a larger search length makes displacement estimation less limited, this flexibility comes at the cost of an increased probability of incorrect peak detection. As a result, in determining the search length, there is also a tradeoff between optimization of the dynamic range and the estimation error.

3.2.2 Coarse-to-Fine Search

As mentioned in Section 2.1, either the raw RF data or the envelopes can be used as templates for displacement estimation, but they present different properties. Envelopes characterize the tissue structure without the high-frequency component inherent in RF data that might interfere with correlation peak detection. Hence, it is more suitable to use envelopes to track large-scale displacement than to use RF data. On the other hand, the additional phase information included in RF data can assist fine-tuning of displacement estimation.

In this displacement estimation algorithm, a coarse-to-fine search approach is designed to utilize the advantages of both using RF data and envelopes. Coarse-scale search is performed by using envelopes with decimated samples. Localized fine-scale search is then performed by using RF data around the location found in coarse scale.

3.2.3 Correlation Filtering

In the correlation-based template matching method, robust peak detection and displacement estimation rely heavily on the signal-to-noise ratio (SNR) of the correlation coefficient functions. To increase the SNR, it is tempting to choose a large correlation kernel, but the amplified intra-kernel deformation effect brings deviation of the correlation peak from the true displacement value.

Lubinski *et al.* proposed a correlation filtering method that allows the use of a short correlation kernel while maintaining a high SNR in the coefficient function. [21] In the coarse-to-fine search scheme, this filtering method is applied in the coarse-scale search to reduce the relatively high probability of error in peak detection resulting from the large search range.

The correlation filtering method is based on the fact that displacement values are similar in the neighborhood of a given location of estimation. See Figure 3-6 for an illustration of this method. At each sample point along the axial direction, a correlation coefficient function is estimated from template matching, as expressed in Equation 3.1. For a given location of estimation *t*, the method weights and sums the correlation coefficient functions from the neighboring points. The synthesized coefficient function $\hat{\rho}(t, t+\tau)$ can be expressed as

$$\hat{\rho}(t, t+\tau) = \int_{-\mathrm{T_h}/2}^{\mathrm{T_h}/2} \mathrm{h}(\varphi) \cdot \rho(t+\varphi, t+\varphi+\tau)\mathrm{d}\varphi, \tag{3.2}$$

subject to the normalization condition

$$\int_{-\mathrm{T_h}/2}^{\mathrm{T_h}/2} \mathrm{h(t)\,dt} = 1, \tag{3.3}$$

where $\mathrm{T_h}$ is the length of the correlation filter. The Hanning window is chosen here as the weighting function $\mathrm{h(t)}$.

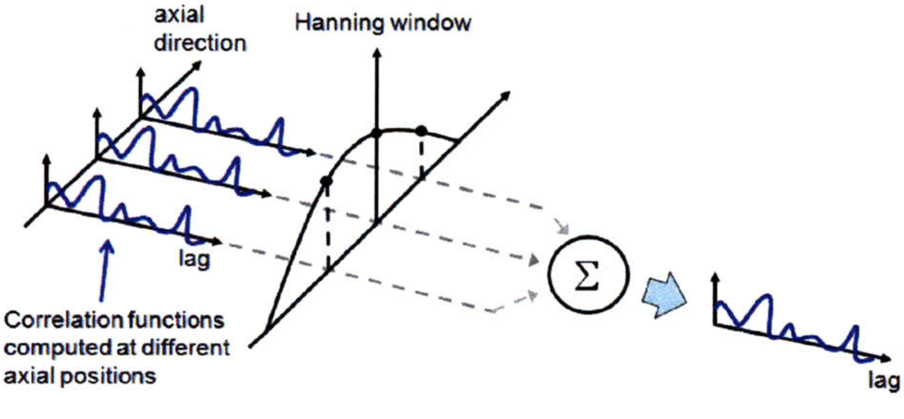

Figure 3-6 Illustration of the correlation filtering method.

There is a tradeoff between choosing a large and a small $\mathrm{T_h}$. Given that the correlation filter includes only correlation coefficient functions that have a peak at the same lag (called "in the same type" subsequently), SNR in the synthesized coefficient function could be increased with $\mathrm{T_h}$. However, if $\mathrm{T_h}$ is increased to such a length that the assumption does not hold, the peak of the synthesized coefficient function might start to deviate from the true displacement value.

The tradeoff is further analyzed in Figure 3-7, where displacement estimation in coarse scale is illustrated (in the coordinate system of the probe.) Under the assumption that the applied stress and tissue elasticity are uniform, the axial strain is almost constant over the depth of interest. The variable *s* denotes the depth range within which the coarse-scale displacement estimates are identical (i.e., the correlation coefficient functions are in the same type.) *h* equals *s* times the strain value. In coarse-scale correlation filtering, if the depth of interest is around the center of one of the "stair levels" and T_h is less than *s*, the included correlation coefficient functions are in the same type. However, in the worst-case scenario, where the depth of interest is near the "stair edge," correlation coefficient functions that are not in the same type are included and the probability of incorrect peak detection could increase.

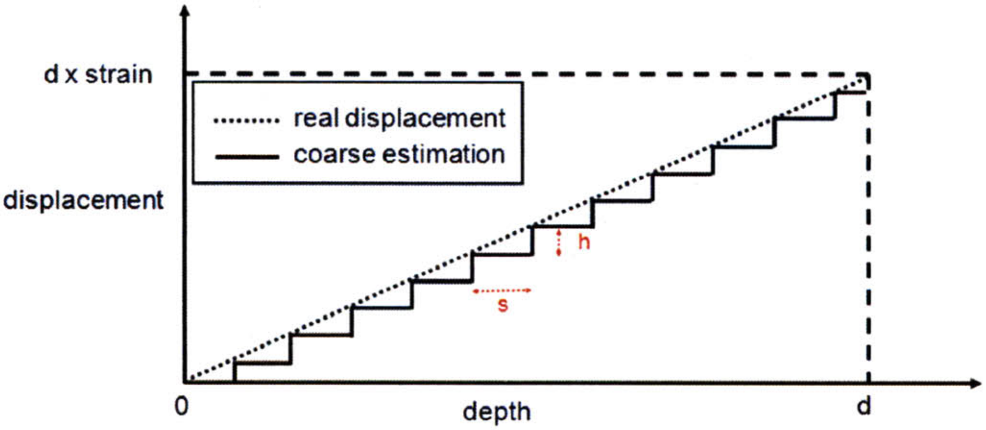

Figure 3-7 Illustration of coarse-scale displacement estimation

To avoid this possible deterioration in the performance of displacement estimation due to coarse-scale correlation filtering, the fine-scale search region is designed to be larger than required. This design is illustrated in Figure 3-8, where red and black dots represent samples in coarse- and fine-scale search, respectively. In this figure, suppose that point A corresponds to the correct location of the overall displacement estimation for a certain depth of interest. Accordingly, in the corresponding coarse-scale search, point B should be selected. In the case where the point D is incorrectly selected in the coarse-scale search, the fine-scale search region around point D still allows point A to be examined in the fine-scale search. In this way, even if incorrect coarse-scale peak detection occurs as in the worst case in Figure 3-7, this error could be corrected in the fine-scale search, as long as the magnitude of error is not greater than one coarse-scale sampling distance.

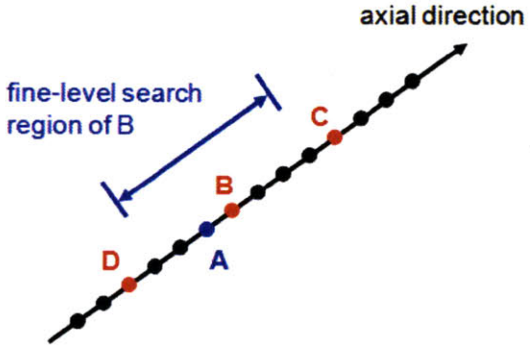

Figure 3-8 Design of the fine-scale search region to reduce possible peak detection errors brought by correlation filtering

Note that since the computation of normalized correlation coefficient functions is highly nonlinear, template matching using a short kernel with correlation filtering is not equivalent to that using a large kernel without filtering. In fact, the equality can be proved to hold if correlation functions instead of correlation coefficient functions are used in template matching. A detailed analysis can be found in the work by Huang *et al.*[22]

3.2.4 Subsample Estimation

The correlation-based template matching technique and the related searching strategies are applicable to displacement estimation in the axial direction, but the spatial resolution of the estimated displacement field is limited by the spatial sampling distance. This limitation becomes even more serious in estimating lateral displacements because in the lateral direction, the spatial sampling distance is even larger and the magnitudes of displacements are generally smaller than those in the axial direction.

To achieve displacement estimation with subsample accuracy, interpolation is performed on the sampled cross correlation coefficient functions. It is based on an iterative 1D estimation scheme, where estimation in the lateral direction is performed at the locations previously found in the corresponding axial displacement estimation, since pixel displacements in the two directions are physically coupled. [19]

Curve fitting through three sample points is used as the interpolation scheme. [20] See Figure 3-9 for an illustration of this procedure. Suppose in fine-scale template matching in the *y*-direction (axial), the position (0, 0) is found to give the maximum sampled correlation coefficient, R(0, 0). By using the neighboring correlation coefficient estimates, R(0, -1) and R(0, 1), the location that gives the maximum of the correlation coefficient function can be found by curve fitting. This location is denoted by (0, δ). For interpolation in the *x*-direction (lateral), the same curve fitting procedure is performed on other neighboring correlation coefficient estimates to find R(-1, δ) and R(1, δ), the coefficient estimates of the neighboring functions. Along with R(0, δ), these estimates are used to compute γ and R(γ, δ), following the same curve-fitting procedure.

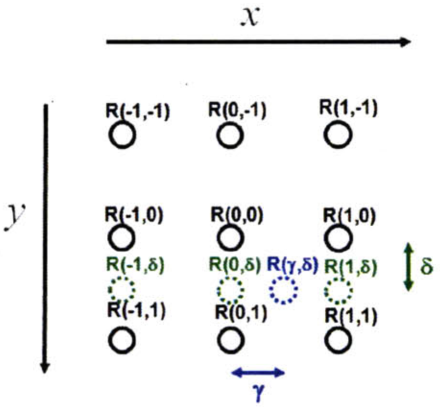

Figure 3-9 Curve fitting using three sample points is applied in two directions for subsample accuracy in displacement estimation

Several types of curve fitting have been developed and evaluated, including parabolic [20] and cosine curve fitting [23]. In previous studies [19], it has been shown that among these strategies, cosine curve fitting gives the best performance in this particular displacement estimation problem, and hence this fitting method is used in this thesis.

The formulas for cosine curve fitting are described in the following. Suppose for the example in Figure 3-9, three coefficient estimates R(0, -1), R(0, 0), and R(0, 1) are to be fitted by a cosine function $\mathrm{R}(0,\mathrm{t}) = \mathrm{a} \cdot \cos(\omega \mathrm{t} + \varphi)$. Since there are three degrees of freedom in the cosine function and three constraints are given by the coefficient estimates, the parameters can be found to be

$$\omega = \cos^{-1}\left(\frac{R(0,-1) + R(0,1)}{2R(0,0)}\right);\ \varphi = \tan^{-1}\left(\frac{R(0,-1) - R(0,1)}{2R(0,0)\sin\omega}\right) \tag{3.4}$$

We can then have

$$\delta = -\frac{\varphi}{\omega};\ R(0,\delta) = a = \frac{R(0,0)}{\cos\varphi} \tag{3.5}$$

Similar computation can be performed to find $R(-1,\delta)$, $R(1,\delta)$, $R(\gamma,\delta)$, and γ.

3.2.5 Smoothing with Non-Uniform Spatial Resolution

The displacement estimation method described above relies heavily on robust peak detection of the correlation coefficient functions. Nonetheless, the performance of peak detection is often deteriorated by noise from various sources, such as an insufficient number of samples in correlation estimation and intra-kernel deformation of the templates. Among the resulting displacement estimation errors, peak-hopping errors are the most visually discernible, which are defined as deviations from the ground truths by at least half of the wavelength of the carrier waveform. A detailed discussion of peak-hopping errors can be found in the work of Weinstein *et al.* [24]

Those errors manifest themselves as "pepper-and-salt" noise in the estimated displacement fields and strain images. This noise could considerably degrade the performance of pixel tracking and interfere with the interpretation of strain images. Median filtering is the standard method to perform smoothing on the noisy results, but this reduction in noise comes at the cost of degrading the spatial resolution.

In fact, median filtering is required only in the region where those artifacts occur, but not in the whole field of view. Figure 3-10 shows simulated axial displacement estimation results and the locations where peak-hopping errors occur (see Chapter 4 for the simulation framework.) Figure 3-11 shows the spatial distribution of the correlation coefficients computed from axial displacement estimation and the locations where the coefficients are lower than the threshold value 0.5. The high correlation between the occurrence of peak-hopping errors and low correlation coefficients is demonstrated through the comparison of Figure 3-10 (b) and Figure 3-11 (b).

Based on this observation, a filtering scheme with non-uniform spatial resolution is proposed to smooth the low-quality estimation results while reserving the spatial resolution in the region of high-quality estimation. The value of correlation coefficient is used as an indicator of the quality of displacement estimation. At the locations of low-quality estimation, 9 × 9 median filtering is applied. Then the whole field of view is smoothed by another 5 × 5 median filtering.

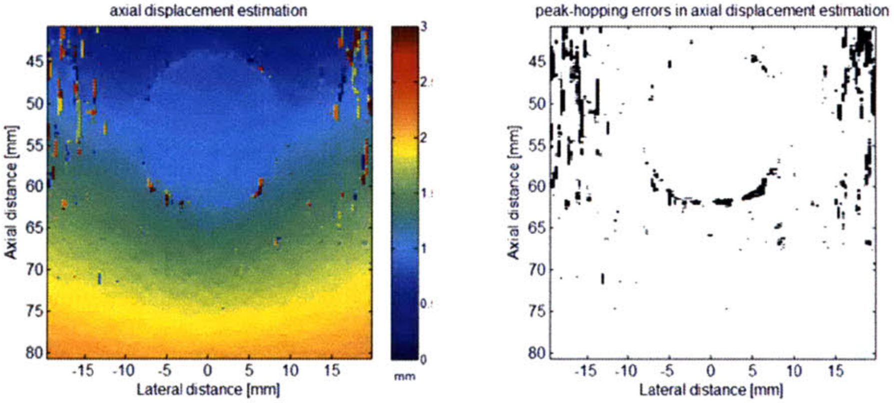

(a)

(b)

Figure 3-10 (a) simulated axial displacement estimation results; (b) the black dots indicate the occurrence of peak-hopping errors in the estimation results

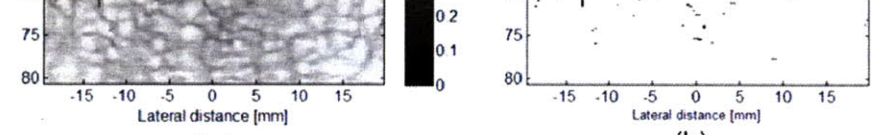

(a)

(b)

Figure 3-11 (a) computed correlation coefficients in axial displacement estimation; (b) the black dots indicate the locations where the correlation coefficients are lower than 0.5

3.3 Polynomial Curve Fitting

After the trajectory field is established from the acquired sequence of ultrasound images, the image under a specified contact force can be estimated from the field. If the specified force lies within the range of the acquired forces, linear interpolation is performed on the trajectories between the two acquired forces that enclose the specified force. On the other hand, if the specified force is beyond the acquired force range, extrapolation is performed on the trajectories.

Here the ordinary least-square curve fitting is used to perform extrapolation. Polynomial curves with varying orders are examined, which can be expressed by Equation (3.6a) and (3.6b)

$$x_{i,j}(f) = \sum_{k=0}^{N} \alpha_{i,j,k} \cdot f^k \tag{3.6a}$$

$$y_{i,j}(f) = \sum_{k=0}^{N} \beta_{i,j,k} \cdot f^k, \tag{3.6b}$$

where $x_{i,j}$ and $y_{i,j}$ are the lateral and axial coordinates, respectively, of the pixel located at the position (i, j) of the reference image. α and β are the parameter sets that are to be determined in the curve fitting procedure. f denotes the contact force and N denotes the order of the polynomial curves.

It is widely reported that, when compressed under a wide range of forces, biological tissue exhibits significant nonlinear mechanical behaviors. [25] Therefore, to characterize the pixel trajectories, polynomial orders up to the number of acquired frames minus one are tested. The results are presented and discussed in Section 4.3.

3.4 Summary

This chapter provided a detailed introduction to the trajectory-based deformation estimation and correction method, which consists of 2D displacement estimation on the acquired ultrasound images and polynomial curve fitting on the established trajectory field. The displacement estimation method is based on a template matching scheme, in which the search is performed using a coarse-to-fine approach. Correlation coefficients are used as the similarity measure, and the correlation filtering method is incorporated to improve correlation estimation. Two-dimensional curve fitting is used to provide subsample estimation accuracy. Finally, a smoothing scheme with non-uniform spatial resolution is proposed to filter out noise while preserving high spatial resolution in regions of high quality estimation.

Chapter 4

Ultrasound Simulation Using Finite-Element Methods

In this chapter, compression of biological tissue and acquisition of the corresponding ultrasound images are simulated by using Finite-Element Methods (FEM) and the ultrasound simulation software Field II [26],[27]. The setup of simulation is described in Section 4.1.

Through the use of the simulated images and the FEM ground truth, performances of displacement estimation, extrapolation by polynomial curve fitting, and deformation correction are examined. These results are presented and discussed in Section 4.2-4.4, respectively.

4.1 Simulation Setup

The simulation framework consists of breast tissue modeling both in FEM and Field II. A numerical tissue phantom was built in FEM to characterize the mechanical behaviors of breast tissue under probe contact. A corresponding phantom was built in Field II for simulating ultrasound images of the numerical phantom in FEM under varying deformation states. Note that although simulation in this chapter is performed assuming that breast tissue is under investigation, the framework described is applicable to any kind of soft tissue.

4.1.1 FEM

A 100 mm × 60 mm numerical phantom that models breast tissue was built in commercial FEM software (Abaqus 6.8, HKS, Rhode Island). Inside the phantom, a circular region with a radius of 7.5 mm was delineated to mimic pathological tissue, and the center was placed 22.5 mm below the top surface of the phantom. The whole phantom was then meshed into 3724 plane strain quadrilateral elements with 3825 nodes, as shown in Figure 4-1. FEM simulation was set to be two-dimensional, that is, in the axial and lateral directions. Deformation of the numerical phantom in the elevational direction is ignored, which is consistent with the assumption in the displacement estimation algorithm

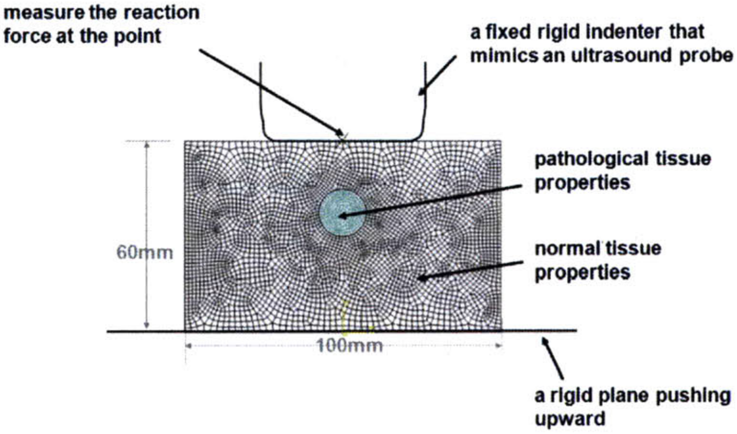
measure the reaction force at the point
a fixed rigid indenter that mimics an ultrasound probe
pathological tissue properties
60mm
normal tissue properties
100mm
a rigid plane pushing upward

Figure 4-1 The setup in FEM

The mechanical behaviors of the phantom undergoing finite strains were characterized by hyperelastic models, as significant nonlinear behaviors of compression on biological tissue are widely found.[25] In addition, the simulated tissue was assumed to be isotropic and incompressible. Out of several hyperelastic models, such as the Neo-Hookean, Mooney-Rivlin, Yeoh, Arruda-Boyce, and Ogden models, the second-order polynomial model was selected as it has been suggested as a good fit of the mechanical behaviors of compressed breast tissue. [28] The model is described by the strain energy function in Equation 4.1.

$$U = \sum_{i+j=1}^{2} C_{ij}(I_1 - 3)^i (I_2 - 3)^j + \sum_{i=1}^{2} \frac{1}{D_i}(J_{el} - 1)^{2i}, \tag{4.1}$$

where U is the strain energy per unit volume, I_1 and I_2 are the first and second deviatoric strain invariant, respectively, and J_{el} is the elastic volume strain. C_{ij}'s are the material parameters with the units of force per unit area, and D_i's are compressibility coefficients that are set to zero for incompressible materials.

In the numerical phantom, normal breast tissue was characterized by the hyperelastic properties of adipose, and pathological tissue by those of low grade invasive ductal carcinoma (IDC), as IDC is the most commonly observed breast cancer. The hyperelastic parameters of those tissue types can be estimated from *ex-vivo* experiments and are reported in [25] and [28]. These parameters are summarized in Table 4-1.

Table 4-1 The hyperelastic parameters of normal and pathological breast tissue in FEM

	C_{10}	C_{01}	C_{11}	C_{20}	C_{02}
Adipose	3.1	3.0	22.5	38.0	47.2
Low grade IDC	30.8	30.8	94.2	94.2	1390

unit: 10^{-4} N mm^{-2}

A rigid indenter mimicking an ultrasound probe (vermon LA 5.0/128-522) was modeled and used to compress the phantom against the rigid plane at the bottom. Compression was performed in a quasi-static manner for describing very slow motion and ignoring inertial effects. It should be noted that, in ultrasound scanning, the subject is scanned with respect to the probe. Therefore, features in the phantom would appear to be moving upward in the image when being compressed, while they would actually move downward physically. In order to describe tissue deformation measured in the coordinate system of the probe, in the simulated compression, the probe was fixed and the rigid plane was set to move upward.

4.1.2 Field II

To simulate the ultrasound images of the numerical phantom in FEM, a corresponding phantom was modeled in the ultrasound simulation software Field II. 2×10^5 scatterers were randomly distributed in a 100 mm × 60 mm × 10 mm cube to simulate the behavior of tissue reflecting ultrasound waves. The top surface of the phantom was set to be 30mm below the probe. A sampled set of the scatterers is shown in Figure 4-2. The circular region marked in blue corresponds to the simulated pathological tissue in FEM and was set to have a higher average of acoustic impedance in Field II. The rectangular region bounded by dashed lines indicates the field of view in the simulated ultrasound scan. The ultrasound images of the numerical phantom in varying deformation states were simulated by relocating the scatterers according to the results of nodal displacement measurement in FEM deformation analysis.

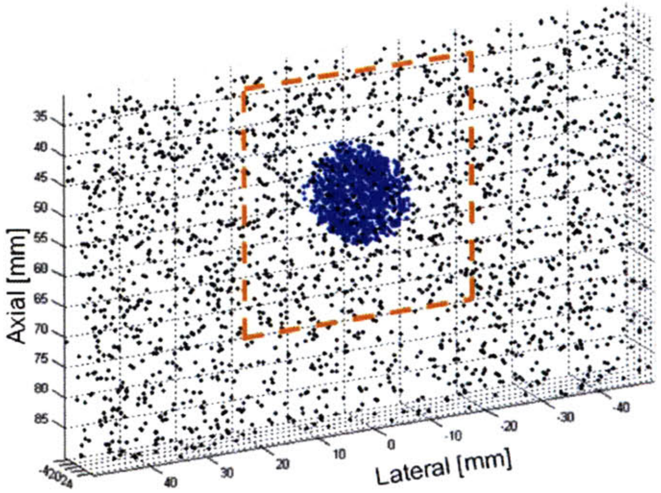

Figure 4-2 A sampled set of the scatterers in ultrasound simulation

Here in the simulation, a linear probe array was modeled, with a center frequency of 5 MHz and a sampling rate of 60 MHz. The transmit focus was set to be 55 mm in depth. The pitch of the probe array was 0.3 mm, and 64 elements were used for every scan line. An image was composed of 128 scan lines, with a spatial spacing of 0.3 mm in the lateral direction.

4.2 Displacement Estimation

The displacement estimation method described in Section 3.2 is evaluated in this section. Specifically, the performance improvement from using the coarse-to-fine search scheme and incorporating correlation filtering are examined through the use of the simulated data. Subsequently, the influence of parameter selection on the performance of displacement estimation is examined.

4.2.1 Single-Level and Coarse-to-Fine Search

Section 3.2 describes a 2D displacement estimation method that incorporates coarse-to-fine search, correlation filtering, and subsample estimation. This particular search scheme is termed "filtered coarse-to-fine" in this section. It is compared with the single-envelope, single-RF, and coarse-to-fine search scheme. Single-envelope and single-RF refer to the single-level correlation-based search scheme that uses envelopes and RF data, respectively, of ultrasound waves for template matching. Coarse-to-fine is the same as the filtered coarse-to-fine scheme except that correlation filtering is not incorporated.

The parameters in each implementation of the search schemes are summarized in Table 4-2. Under the simulation setup, the axial search length of 3 mm corresponds to a maximum detectable strain of 5%. For single-envelope and single-RF, the search is performed on the original spatial resolution as in RF data acquisition, with a sample spacing of around 12.8 μm. For the coarse-to-fine scheme, 4-to-1 decimated samples with a spacing of around 50 μm are used in coarse scale, and the original resolution is used for fine scale. Note that given these parameter settings, the computational cost for the coarse-to-fine search schemes is less than 10% of that for single-level search.

Table 4-2 Parameters for the search schemes

search scheme	parameter	# samples	value (mm)
single-envelope	kernel length	311	4
	axial search length	234	3
single-RF	kernel length	311	4
	axial search length	234	3
coarse-to-fine	kernel length (coarse)	77	4
	axial search length (coarse)	58	3
	kernel length (fine)	155	2
	axial search length (fine)	7	0.09
	correlation filter length	29	1.5

In addition, to examine the influence of noise on the performance of each search scheme, three major sources of waveform decorrelation are modeled. They are:

1. *Applied strain*: when the strain becomes larger, the intra-kernel deformation effect between pre- and post-compression waveforms becomes more prominent, thus making it less appropriate to approximate displacement estimation as a time delay

problem. The examined strain levels are from 1% to 5%, with a spacing of 1%.

2. *Elevational offset*: the spatial shift of the probe in the elevational direction introduces decorrelation between the pre- and post-compression waveforms. The examined elevational offsets are from 0 to 0.4 mm, with a spacing of 0.1 mm.
3. *Signal-to-noise ratio (SNR)*: the quality of signal could also be influenced by other factors, such as the thermal noise inherent in the hardware, the reverberation of ultrasound waves, patient motion artifacts, and so on. They are collectively modeled as additive white Gaussian noise (AWGN) in this analysis. The examined SNR levels are from 10 dB to 50 dB, with a spacing of 10 dB.

In the above framework, the estimation accuracy and robustness of each search scheme are compared. The accuracy is quantified by the mean absolute errors (MAE) between the displacement estimation results and the FEM ground truth. The robustness is characterized by the occurrence rates of the axial peak-hopping error, which is defined as an error larger than half of the carrier wavelength. At each noise setup in the following analysis, each search scheme was evaluated 25 times. For each independent trial, there was a different realization of the ultrasound simulation (i.e. different random locations of Field II scatterers) and random AWGN. The curves indicate the mean values of the results, and the error bars indicate one standard deviation.

Figure 4-3 shows the change in MAE and peak-hopping errors with the applied strain level in axial displacement estimation. The elevational offset is set to be zero, and SNR is set to be 30 dB. As expected, when the strain becomes larger, estimation is more error-prone for all the examined schemes. Nevertheless, it is obvious that the coarse-to-fine search scheme is more accurate and robust than single-level search in the presence of a high strain level, and coarse-scale correlation filtering brings noticeable improvement in displacement estimation. Similar observations can be made from analysis of elevational offsets (Figure 4-4), where the strain level is set to be 2% and SNR is set to be 30 dB.

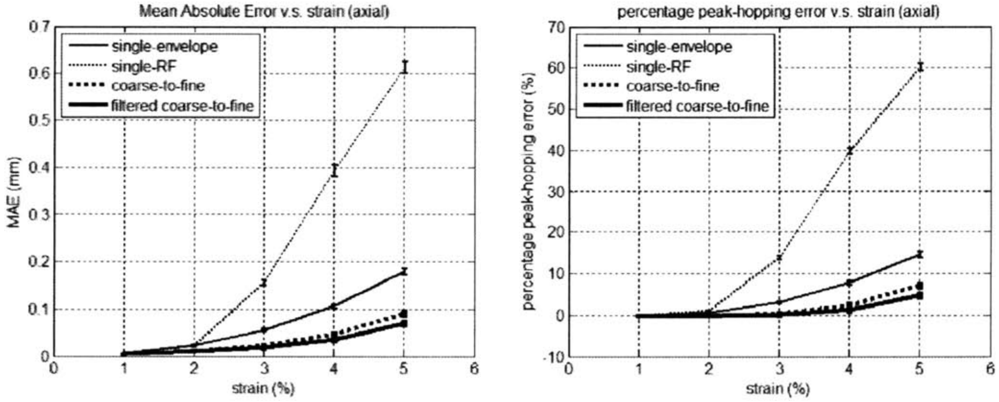

(a) (b)

Figure 4-3 The axial displacement estimation MAE (a) and peak-hopping errors (b) versus the applied strain

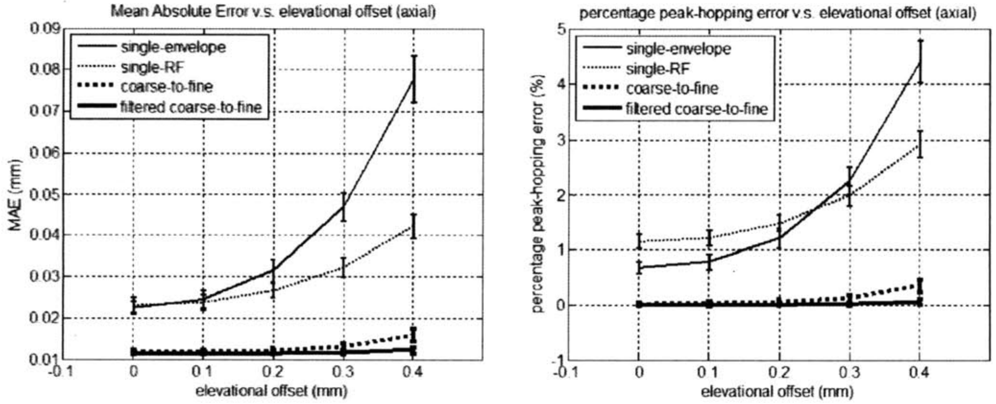

(a) (b)

Figure 4-4 The axial displacement estimation MAE (a) and peak-hopping errors (b) versus the probe elevational offset

Figure 4-5 shows the change in MAE and peak-hopping errors with SNR in axial displacement estimation, where the strain level is set to 2% and the elevational offset is set to 0. At a SNR higher than 10 dB, coarse-to-fine search schemes give better performance than single-level schemes. Even when SNR is as low as 10 dB and single-level search using RF data outperforms coarse-to-fine search, the addition of correlation filtering to the coarse-to-fine search scheme still brings significant improvement and gives the minimum estimation errors.

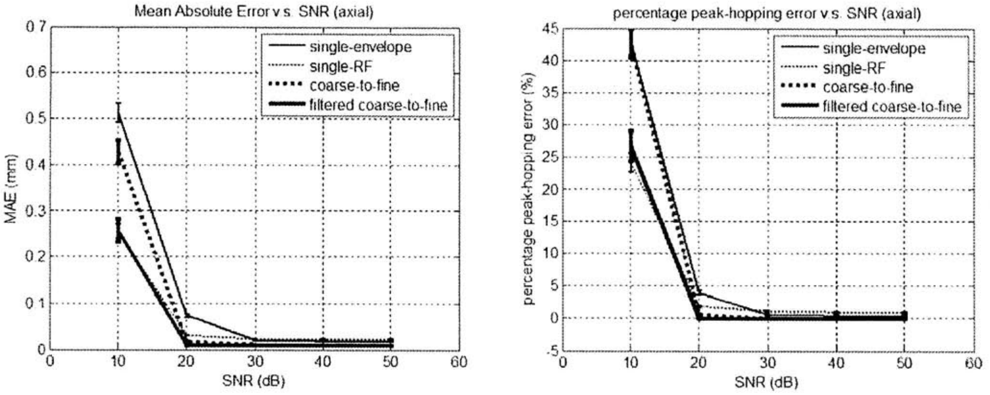

(a) (b)

Figure 4-5 The axial displacement estimation MAE (a) and peak-hopping errors (b) versus SNR

From the above results, it has been shown that in axial displacement estimation, the coarse-to-fine approach, combined with correlation filtering, outperforms other search schemes under comparison. However, this is not the case in estimating lateral displacements. As shown in Figure 4-6, this particular approach is inferior to the single-level search scheme using envelopes, and has similar performance as other schemes in estimating lateral displacements.

It should not be surprising that the single-level envelope scheme has significantly different behaviors than the other three in lateral estimation, since it is the only search scheme that uses envelopes to compute fine-scale correlation coefficients, on which the estimation of lateral displacements solely depends as described in Section 3.2.4. The results imply that, in the 2D curve-fitting framework, lateral displacements of tissue under compression are more suitably characterized by envelopes, since the phase information inherent in the RF data can not contribute directly to lateral estimation.

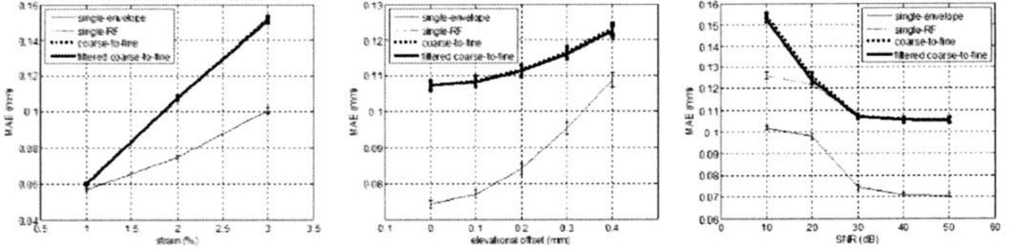

(a) (b) (c)

Figure 4-6 The lateral displacement estimation MAE versus the strain (a), elevational offset (b), and SNR (c)

Given the above comparison, the selection of a particular search scheme should depend on the specific application of displacement estimation. Since in this thesis, displacement estimates are used for modeling tissue deformation under probe compression, where tissue movements in the axial direction are predominant, the coarse-to-fine approach combined with correlation filtering is the most suitable.

4.2.2 Analysis of Parameter Selection

In Section 3.2, the tradeoffs in selecting parameters in the filtered coarse-to-fine scheme are described. In this section, the influences of three parameters on the performance of displacement estimation are demonstrated and discussed through simulation. These parameters include the kernel length in coarse scale, the kernel length in fine scale, and the correlation filter length in coarse scale. In the following analyses, if not otherwise specified, the selection of the parameters is as summarized in Table 4-2. At each parameter setting in the following analysis, estimation at each strain level was evaluated 25 times. For each independent trial, there was a different realization of the ultrasound simulation (i.e. different random locations of Field II scatterers) and random AWGN. The curves indicate the mean values of the results, and the error bars indicate one standard deviation.

Figure 4-7 shows the change of displacement estimation errors with the coarse-scale kernel length under strain levels of 1% to 5%. As expected, errors are large at the two ends of the curves, since too small a kernel length gives a small sample volume and makes correlation estimation less robust, and too large a length amplifies the intra-kernel deformation effects. The minima of the curves occur at kernel lengths around 4 mm and 5 mm.

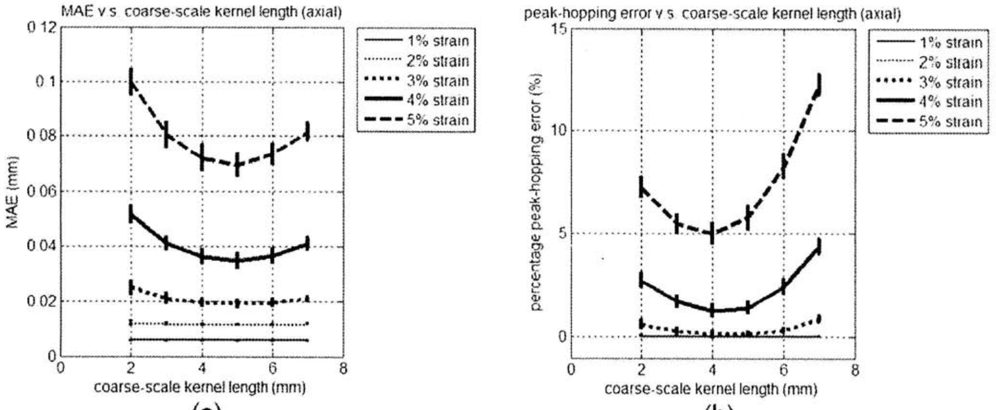

(a)

(b)

Figure 4-7 The axial displacement estimation MAE (a) and peak-hopping errors (b) versus the coarse-scale kernel length

Figure 4-8 shows the change of displacement estimation errors with the fine-scale kernel length, where the trends of the curves in (a) and (b) are in opposite directions. This observation implies that, in the range of kernel lengths under investigation, MAE is more sensitive to the intra-kernel deformation effect, while the peak-hopping error rate is more sensitive to the sample volume in estimation of correlation coefficients. This should not be surprising, since intra-kernel deformation normally brings moderate increase in estimation errors, which is characterized only by MAE, while a small sample volume in estimating correlation coefficients could lead to peak detection errors large enough to be considered peak-hopping errors. The different trend of MAE from that of the peak-hopping error rate also indicates the limited scope of influence of fine-scale search on peak-hopping errors. This results from the fact that the search length in fine scale is much smaller than that in coarse scale, and hence there is little room for influencing the peak-hopping error rate.

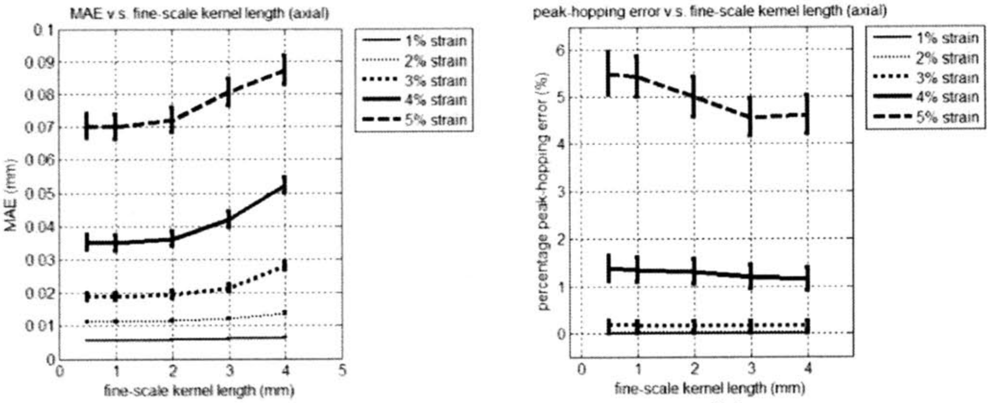

(a) (b)

Figure 4-8 The axial displacement estimation MAE (a) and peak-hopping errors (b) versus the fine-scale kernel length

Figure 4-9 shows the change of displacement estimation errors with the coarse-scale filter length. It can be seen that as the filter length increases, both the MAE and peak-hopping errors decrease. This phenomenon can be explained by Figure 3-7, where the coarse-scale displacement estimation is illustrated. Note that in this simulation setup, the spacing between neighboring coarse-scale samples is about 0.05 mm, which is denoted by h in the displacement-depth plot in Figure 3-7. Under a strain level less than 5%, the variable s in Figure 3-7 is larger than 1mm. In other words, the correlation filter lengths investigated in Figure 4-9 are less than $2s$, which makes the possible errors brought by coarse-scale correlation filtering recoverable in fine scale, as explained in Section 3.2.3. As a result, in the scope of this analysis, correlation filtering improves the quality of correlation estimation without deteriorating peak detection.

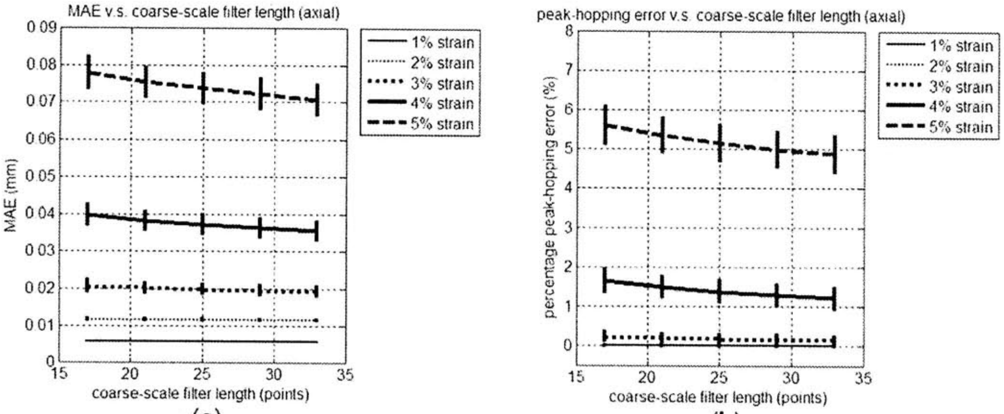

(a) (b)

Figure 4-9 The axial displacement estimation MAE (a) and peak-hopping errors (b) versus the coarse-scale correlation filter length

Figure 4-10 shows change in the performance of lateral displacement estimation with the three parameters. The results imply that the estimation is not severely influenced by the performance in coarse-scale search, but heavily relies on the fine-scale correlation coefficient estimates. In Figure 4-10 (b), the increase of MAE with the fine-scale kernel length also implies that, in the estimation of subsample lateral displacement, the accuracy is markedly sensitive to the intra-kernel deformation effect.

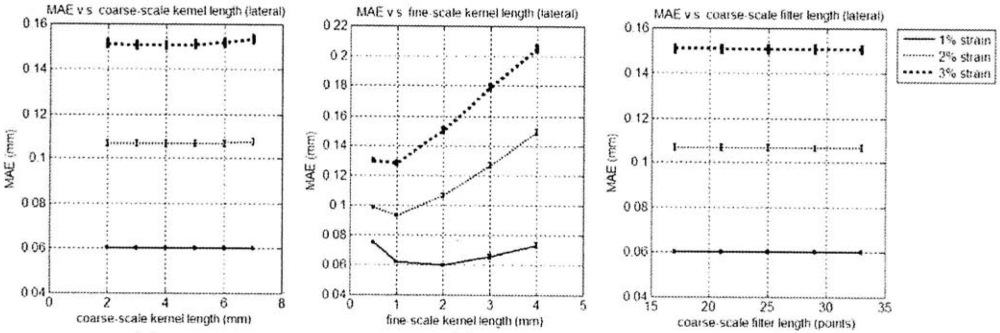

(a) (b) (c)

Figure 4-10 The lateral displacement estimation MAE versus the coarse-scale kernel length (a), the fine-scale kernel length (b), and the coarse-scale filter length (c)

4.3 Curve Fitting

After the trajectory field of the acquired ultrasound images is established by displacement estimation, extrapolation is performed by polynomial curve fitting through the trajectories for correcting tissue deformation. In this section, the performance of extrapolation is investigated under a control-force scenario, where the applied force onto the skin surface can be controlled by a mechanically actuated probe. [29]

Selection of the constituent frames in the trajectory field is one of the crucial factors to the performance of extrapolation. Since the main purpose of extrapolation is to project the trajectories back to zero force, all the frames should be acquired under contact forces close to zero. However, the resolution of force control is limited, mainly by the given force sensor and mechanical design of the probe. Therefore, force sampling in this thesis starts from the minimal discernible force and continues increasingly with force spacing equal to the resolution. For instance, for a force resolution of 20 mN, the images will be acquired under forces of 20 mN, 40 mN, 60 mN, and so on.

Under this strategy, it is expected that there are tradeoffs in determining both the number of constituent frames and the order of the fitting polynomial curve. With too few frames, the hyperelastic behaviors of tissue compression might not be fully characterized, but too many frames far from zero force might interfere with the behaviors one wish to model and induce unnecessary computational cost from displacement estimation. Similarly, a low order might fail to fully characterize the hyperelastic behaviors, while a high-order polynomial tends to be less resistant to noise in curve fitting, due to the overfitting effect. In the following analysis, the influences of the number of frames and polynomial order are further investigated.

4.3.1 Noise Modeling in Displacement Estimation

In this analysis, the force resolution is assumed to be 20 mN, 50 mN, or 100 mN. For each resolution, two to eight frames are acquired for extrapolation, as illustrated in Figure 4-11. To build the trajectory field corresponding to each pair of force resolution and number of frames, the displacement estimates are modeled based on the FEM ground truth through Equation 4.1.

$$\boldsymbol{d'} = d \times \boldsymbol{n_f} + \boldsymbol{n_a}, \tag{4.1}$$

where d is the ground truth displacement at a particular point between two specified contact forces, and d' is the displacement estimate. n_f is the multiplicative noise induced by the inaccuracy in force control, and n_a is the additive noise from the inaccuracy of displacement estimation.

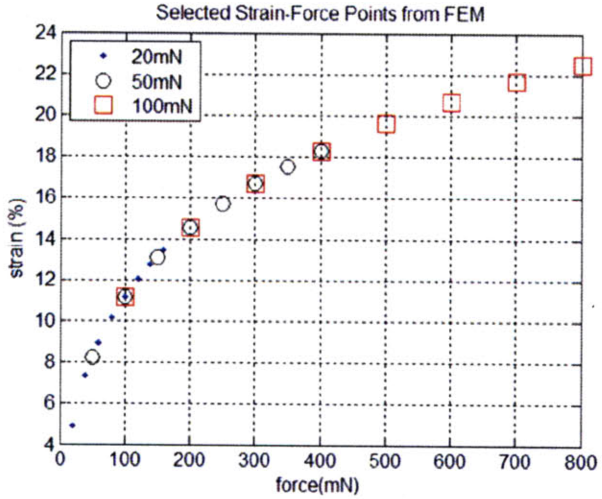

Figure 4-11 Selected strain-force points for varying force resolutions: 20mN, 50mN, and 100mN

The estimation of n_f is illustrated in Figure 4-12, in which the displacement-force curve from the FEM simulation is shown. Suppose that two forces f1 and f2 are set to be applied and the corresponding images acquired. Due to noise in force control, the real applied forces and compression levels might deviate from those that are specified. n_f represents the ratio between the displacements from the real applied forces and the specified forces, and could be estimated from the displacement-force curve in the FEM simulation. Here the force noise is modeled as a Gaussian random variable with zero mean. The standard deviation relates to the specified force resolution and is estimated through the half-maximum criterion, as in Equation 4.2,

$$\sigma = \frac{\rho}{2\sqrt{2ln2}}, \tag{4.2}$$

where σ denotes the standard deviation and ρ denotes the force resolution. Note that under the assumption of tissue incompressibility and constrained elevational movement, the same estimated ratio $\boldsymbol{n_f}$ is applicable to both the axial and lateral displacements.

$\boldsymbol{n_a}$ is also modeled as a Gaussian random variable and separately estimated for axial and lateral displacements. The means and standard deviations of the Gaussian distributions are estimated by comparing the FEM ground truth with the displacement estimation results between the ultrasound images under the specified forces.

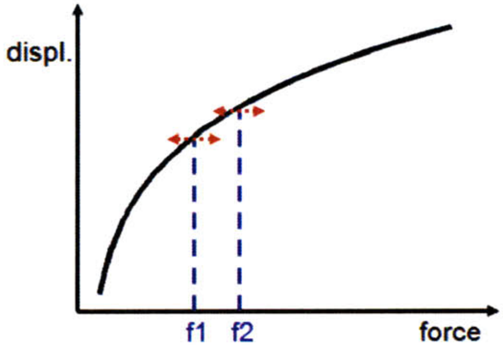

Figure 4-12 Illustration of displacement error induced by noise in force control

4.3.2 Analysis of Parameter Selection

In the simulation framework described above, the relationship between the projection MAE and polynomial orders was investigated for each pair of force resolution and number of frames used. For each pair, polynomial curve fitting with an order of one up to the number of used frames minus one was evaluated 100 times. At each individual trial, different realizations of the random variables $\boldsymbol{n_a}$ and $\boldsymbol{n_f}$ are used. The MAE is computed from comparing the FEM ground truth and the results of projection back to zero force.

Figure 4-13 shows a typical example of the relationship between the MAE and the polynomial order, where eight frames are used with a force resolution of 100 mN. The curve indicates the mean of MAE, and error bars indicate one standard deviation. It appears that the 3rd- and 4th-order give a smaller average MAE than 1st- and 2nd-order. However, note that as a higher order is used, the variance of MAE tends to be larger. Therefore, in determining the polynomial order, there is a tradeoff between minimization of the average projection error, measured by the mean of MAE, and maximization of the projection robustness, measured by the inverse variance of MAE.

Here the verification is focused on minimizing the average MAE. For each pair of force resolution and number of frames, the smallest order that gives the minimal average MAE is chosen under the criterion of statistical significance, which is tested through the student's t-test with a threshold p-value of 0.05. This order is termed the "efficient order" of the particular pair, and the efficient orders for all the pairs are summarized in Table 4-3.

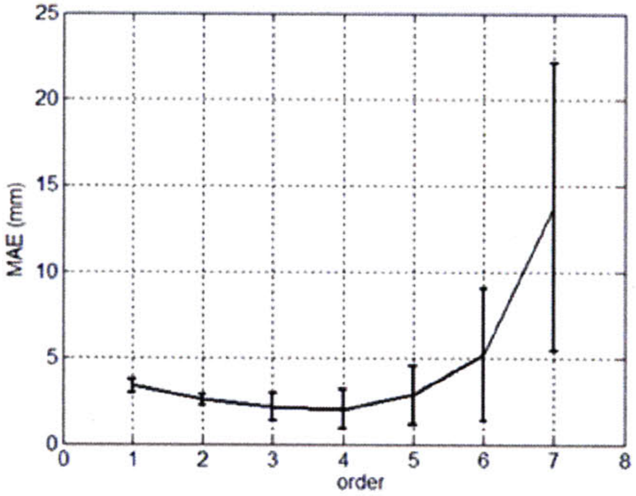

Figure 4-13 Projection MAE versus the polynomial order: eight frames with a 100mN resolution

Table 4-3 The efficient orders for each pair of force resolution and number of frames

		# frames used						
		2	**3**	**4**	**5**	**6**	**7**	**8**
force resolution	**20mN**	1	1	2	2	2	2	3
	50mN	1	2	2	2	3	3	3
	100mN	1	2	2	2	3	3	3

To give the best projection performance while maintaining low computational cost for a given force resolution, the performance by using varying numbers of frames and the corresponding efficient orders are compared. Figure 4-14 shows this comparison for each force resolution. It can be seen that the projection performance improves with a finer force resolution. In addition, the smallest number of frames that gives the minimal average MAE under the criterion of statistical significance is considered the most efficient for the specific force resolution. The numbers and the corresponding efficient orders are summarized in Table 4-4.

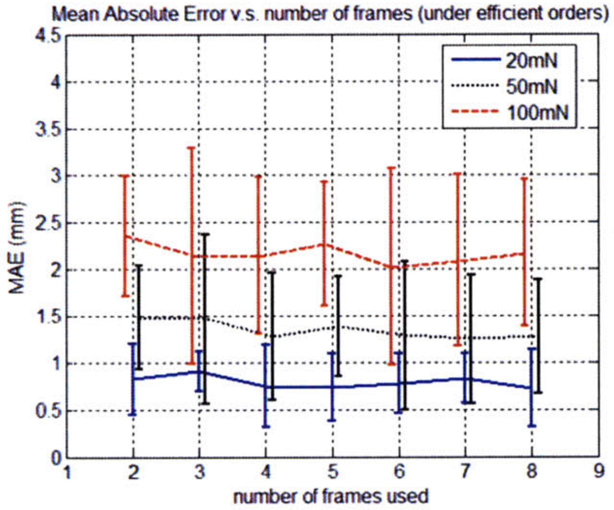

Figure 4-14 Projection performance versus the number of frames used for varying force resolutions

Table 4-4 The most efficient number of frames and the corresponding efficient order for each force resolution

force resolution	number of frames	efficient order
20mN	4	2
50mN	4	2
100mN	3	2

4.4 Deformation Estimation and Correction

In this section, the deformation correction method is applied to the simulated B-mode and elastography images. The performance is examined through comparison of the corrected, uncorrected, and uncompressed contours of the simulated pathological inclusion. The contours were extracted by the Gradient Vector Flow for Snake

(GVF-snake) algorithm. [30],[31] The GVF algorithm uses diffusion of the gradient vectors derived from gray-level edge maps as an external force for active contour fitting. The snakes were initialized using an interactive graphical user interface (GUI), and then gradually shrunk to delineate the edges of the inclusions by iteration. The squared magnitudes of the gradient fields derived from the images were used as the edge maps. The GVF-snake algorithm has been shown to be relatively insensitive to contour initialization and to be able to converge to boundary concavities.

In the following, the results of deformation correction with a force resolution of 100 mN are demonstrated. Subsequently, the performances obtained from using force resolutions of 20 mN, 50 mN, and 100 mN are compared and discussed.

4.4.1 Deformation Correction with 100mN Force Resolution

According to the analysis in Section 4.3, when the force resolution is 100 mN, deformation correction can be performed most efficiently (in the sense of statistical significance) with three frames and second-order polynomial curve fitting, as also summarized in Table 4-4. Therefore in this section, simulated ultrasound images under 100 mN, 200 mN, and 300 mN compression are used to build the trajectory field, and extrapolation is performed with second-order polynomial curves. Note that although an arbitrary selection out of the three images could be used for estimating the uncompressed inclusion appearance, the results of correcting the image under 300 mN compression, which corresponds to a strain of about 17%, are shown here as an example.

Figure 4-15 shows the correction results, where the crosses in (d) indicate the respective centers of area of the contours. The position of the compressed inclusion deviates significantly from that of the inclusion in the uncompressed state. This deviation is characterized by the translational offset of the center of area, as summarized in Table 4-5. From both Figure 4-15 and Table 4-5, it can be seen that this translational deviation is remedied after correction.

The improvement in estimating the uncompressed inclusion contour is quantified by three parameters that characterize area estimation errors: true positive (TP), false negative (FN), and false positive (FP). [32] The computation of those parameters is illustrated in Figure 4-16, and the computed values of the contours are also summarized in Table 4-5. After correction, it can be seen that the probability of correct area estimation increases, and probability of error decreases.

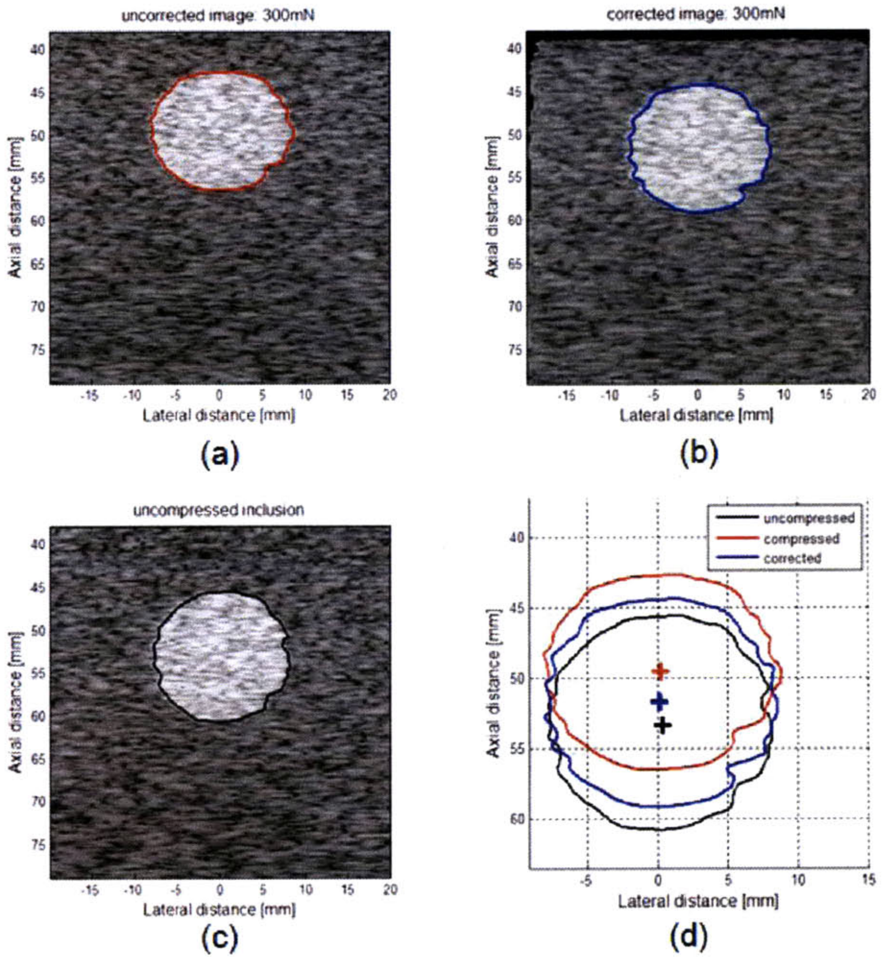
uncorrected image: 300mN
corrected image: 300mN
uncompressed inclusion
Axial distance [mm]
Lateral distance [mm]
40
45
50
55
60
65
70
75
-15
-10
-5
0
5
10
15
20
uncompressed
compressed
corrected
(a)
(b)
(c)
(d)

Figure 4-15 The B-mode image of the 300 mN-compressed inclusion (a) is corrected (b). From the comparison between (a), (b) and the true uncompressed inclusion contour (c), it is shown that the deviation in the position of the inclusion can be remedied. (d)

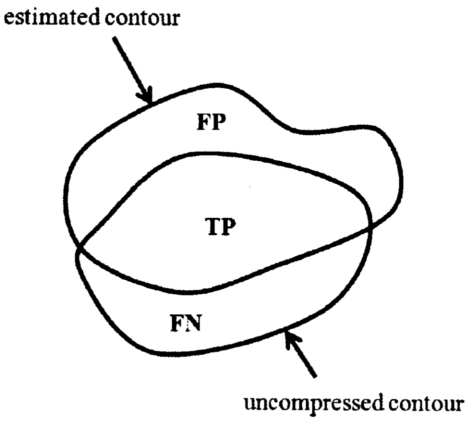

A_{true}: area enclosed by the uncompressed contour
A_{est}: area enclosed by the estimated contour

$$TP = \frac{|A_{true} \cap A_{est}|}{A_{true}}$$

$$FP = \frac{|A_{true} \cup A_{est} - A_{true}|}{A_{true}}$$

$$FN = \frac{|A_{true} \cup A_{est} - A_{est}|}{A_{true}}$$

Figure 4-16 The performance of deformation correction is quantified by three parameters that are derived from area estimation. They are true positive (TP), false positive (FP), and false negative (FN).

Table 4-5 Performance of correcting the B-mode image contour under 300 mN compression as measured by the translational offset from the true uncompressed contour and the area estimation parameters

	translational offset	**area estimation parameters**		
		TP	**FP**	**FN**
uncorrected	3.88 mm	66.75%	28.32%	33.25%
corrected	1.73 mm	87.32%	13.32%	12.68%

The deformation correction procedure and performance analysis were also applied to elastography images. From the above compression sequence, 100-200 mN and 200-300 mN elastography images were acquired. Here the 200-300 mN elastography image is corrected as an example. The correction results are compared with the uncompressed B-mode image since the true uncompressed elastography is not obtainable even in simulation. The contours are demonstrated in Figure 4-17, and the metrics of contour correction are summarized in Table 4-6. Again, after correction, the performance metrics improve significantly. Note that the TP and FP values from elastography correction are significantly higher than those from B-mode image correction, and the FN value is lower. This phenomenon is due to the fact that the inclusion shown in elastography is normally larger than that in B-mode imaging, which results from template-based displacement estimation.

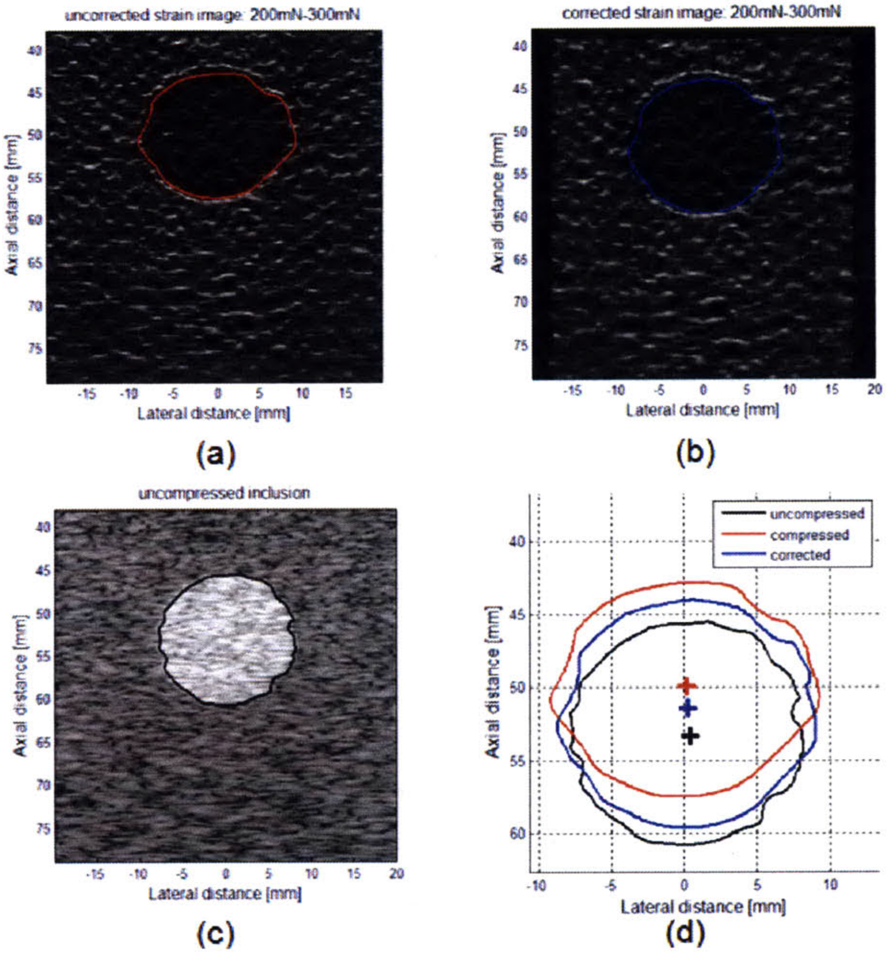
uncorrected strain image: 200mN-300mN
corrected strain image: 200mN-300mN
uncompressed inclusion
Axial distance [mm]
Lateral distance [mm]
40
45
50
55
60
65
70
75
-15
-10
-5
0
5
10
15
20
uncompressed
compressed
corrected
(a)
(b)
(c)
(d)

Figure 4-17 The elastography image under 200-300 mN compression (a) is corrected (b). From the comparison between (a), (b) and the true uncompressed inclusion contour (c), it is shown that the deviation in the position of the inclusion can be remedied. (d)

Table 4-6 Performance of correcting the elastography image contour under 200-300 mN compression as measured by the translational offset from the true uncompressed contour and the area estimation parameters

	translational offset	**area estimation parameters**		
		TP	**FP**	**FN**
uncorrected	3.48 mm	74.87%	30.00%	25.13%
corrected	1.91 mm	91.69%	18.08%	8.31%

4.4.2 Comparison of Force Resolutions

In this section, the performances of correcting 100 mN compression using 20 mN, 50 mN, and 100 mN force resolutions are compared. According to Table 4-4, ultrasound images under 50, 100, 150, and 200 mN were simulated for 50 mN force resolution, and those under 100, 200, and 300 mN for 100 mN resolution. Both the polynomial orders were two. For the 20 mN force resolution, images under 20, 40, 60, 80, and 100 mN compression were used, and according to Table 4-3, second-order polynomial curves were used.

The corrected and the true uncompressed contours are shown in Figure 4-18, in which the crosses indicate the respective centers of area of the contours. It can be seen that when a finer force resolution is available, the translational offset of the center decreases and the corrected contour better approximates the true uncompressed contour. These observations are quantified by the performance metrics of the contours, as summarized in Table 4-7. The superiority of using a finer force resolution is further visualized in Figure 4-19, which shows the absolute values of the pixel-wise difference between the corrected images and the true uncompressed image. It should be emphasized that the observation that a finer force resolution gives better correction results agrees with the conclusions from the analysis in Section 4.3.2.

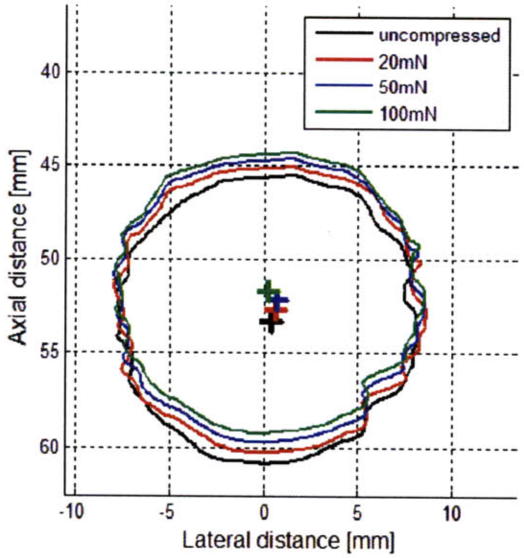

Figure 4-18 Deformation correction of B-mode images: compare 20 mN, 50 mN, and 100 mN force resolution

Table 4-7 Performance of correcting the B-mode image contour under 100mN compression using 20 mN, 50 mN, and 100 mN force resolution as measured by the translational offset from the true uncompressed contour and the area estimation parameters

force resolution	**translational offset**	**area estimation parameters**		
		TP	**FP**	**FN**
20 mN	0.64 mm	95.58%	6.90%	4.42%
50 mN	1.18 mm	91.14%	10.05%	8.86%
100 mN	1.63 mm	87.30%	13.09%	12.70%

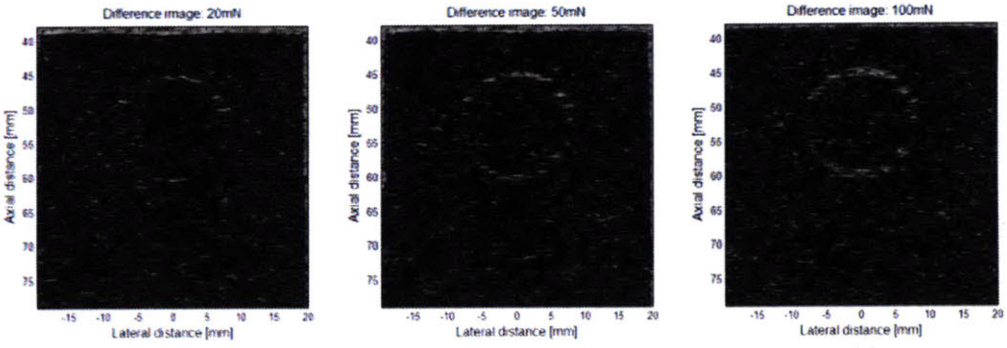

(a) (b) (c)

Figure 4-19 Difference images between the corrected B-mode images and the true uncompressed image using 20 mN, 50 mN, and 100 mN force resolution

The correction performances in elastography obtained by using 20 mN, 50 mN, and 100 mN force resolutions are also examined. Here, 100 mN compression was used as the reference state in acquiring elastography. This image was compared with the images under 120 mN, 150 mN, and 200 mN compression to obtain the displacement field and the resulting strain images. For 50 mN and 100 mN resolution, the number of frames and the polynomial order remained the same as in the above analysis of B-mode images. For 20 mN resolution, 20-120 mN compression images were simulated to build the trajectory field, with a spacing of 20 mN, and second-order polynomial curves were used according to Table 4-3.

The comparison of the contours in elastography is shown in Figure 4-20. With a finer force resolution, the center of area of the corrected contour is closer to that of the true uncompressed contour. The performance metrics computed from those corrected contours are summarized in Table 4-8. Again, it is shown that a finer force resolution gives better performance in contour correction.

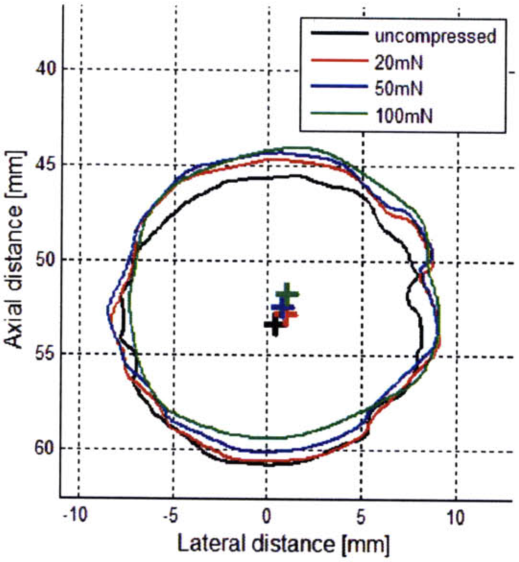

Figure 4-20 Deformation correction of elastography: compare 20 mN, 50 mN, and 100 mN force resolution

Table 4-8 Performance of correcting the elastography image contour under 100-(120 mN, 150 mN, 200 mN) compression using 20 mN, 50 mN, and 100 mN force resolution as measured by the translational offset from the true uncompressed B-mode image contour and the area estimation parameters

force resolution	**translational offset**	**area estimation parameters**		
		TP	**FP**	**FN**
20 mN	0.76 mm	98.77%	12.68%	1.23%
50 mN	1.02 mm	94.88%	14.96%	5.12%
100 mN	1.72 mm	90.52%	15.51%	9.48%

4.5 Summary

This chapter presented a simulation framework that incorporates FEM and ultrasound simulation. Performances of displacement estimation, extrapolation using polynomial curve fitting, and deformation correction are examined in this framework. It has been shown that, in axial displacement estimation, the coarse-to-fine scheme performs better than single-level search, and incorporation of correlation filtering brings noticeable improvement. The influences of parameter selection in the filtered coarse-to-fine scheme are also examined. For extrapolation using polynomial curve fitting, the most efficient selection of the number of frames and the corresponding polynomial order is found for a force resolution of 20 mN, 50 mN, and 100 mN. Finally, deformation correction applied to both B-mode imaging and elastography is validated through simulation, and it is verified that a finer force resolution gives better performance.

Chapter 5

In-Vitro Experiments

In this chapter, the performance of the proposed deformation correction method applied to a tissue phantom object is verified. In Section 5.1, the experiment setup is described. In Section 5.2, the experiment results are presented and discussed.

5.1 Experiment Setup

In this *in-vitro* experiment, the commercial breast ultrasound needle biopsy phantom (Model 052A, CIRS, Virginia) was used to validate the deformation correction method. The volume of the phantom is about 600 cm^3. Six cysts and six solids of varying sizes are embedded at random locations in the phantom, as illustrated in Figure 5-1. Note that this phantom provides a subject to examine the tissue deformation effects and to validate the deformation correction method, but the elastic properties of this phantom do not emulate those of real breast tissue.

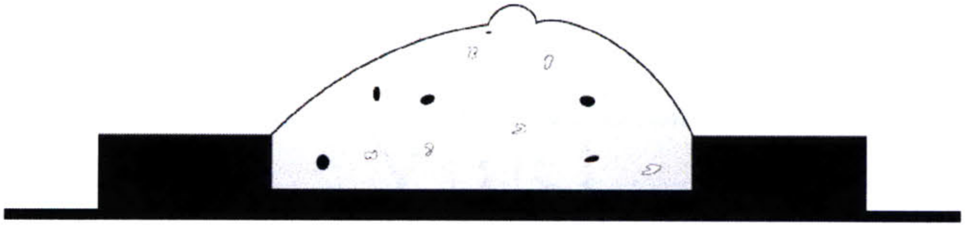

Figure 5-1 The breast ultrasound needle biopsy phantom used in the *in-vitro* experiment (from http://www.cirsinc.com/)

The experiment setup is shown in Figure 5-2. A novel force-controlled ultrasound probe was used to control the contact force applied in scanning the phantom [29], and the ultrasound images were acquired by using the Terason t3000 ultrasound imaging system. [8] In the following, the force-controlled probe and the image acquisition system are detailed.

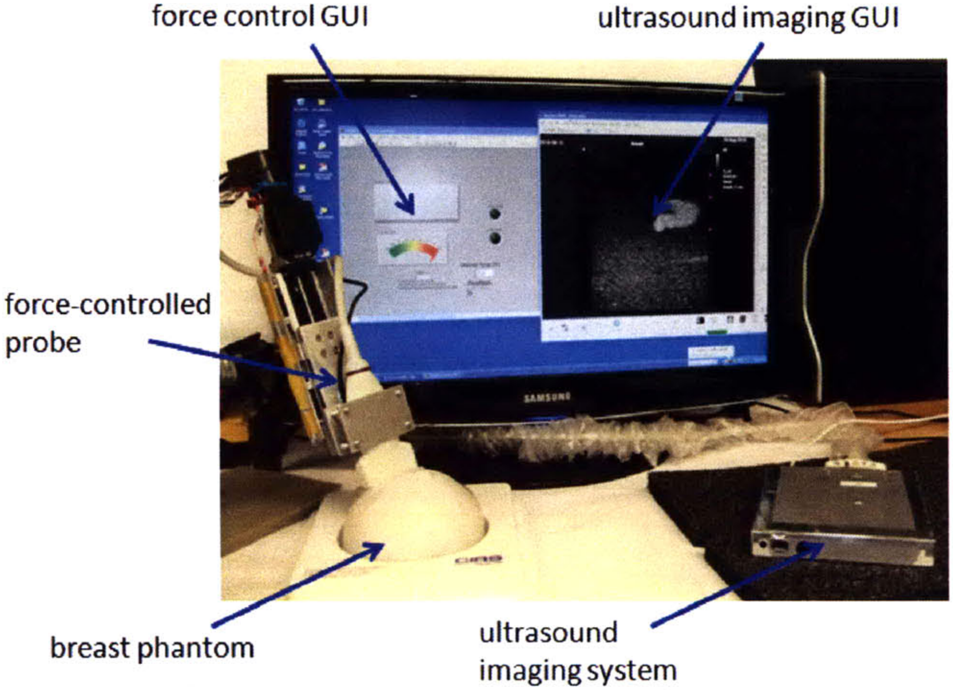
force control GUI
ultrasound imaging GUI
force-controlled probe
breast phantom
ultrasound imaging system

Figure 5-2 The *in-vitro* experiment setup

5.1.1 Force-Controlled Ultrasound Probe

In order to accurately control the contact force in an ultrasound scan, a novel robotic probe system was developed. [29] The hardware is shown in Figure 5-3. The contact force is measured by a six-axis force/torque sensor. Based on this measurement, the servo motor moves the probe to a position where the specified contact force is achieved. The gravitational effects are compensated by an orientation sensor. Figure 5-4 shows the graphical user interface (GUI) of the force control system, which is built using LabVIEW (National Instruments, Austin, Texas). This system provides a force resolution of 100 mN. By using this probe with a mounting system (Manfrotto 143N Magic Arm), a sequence of ultrasound images can be acquired at the same scan plane under varying contact forces.

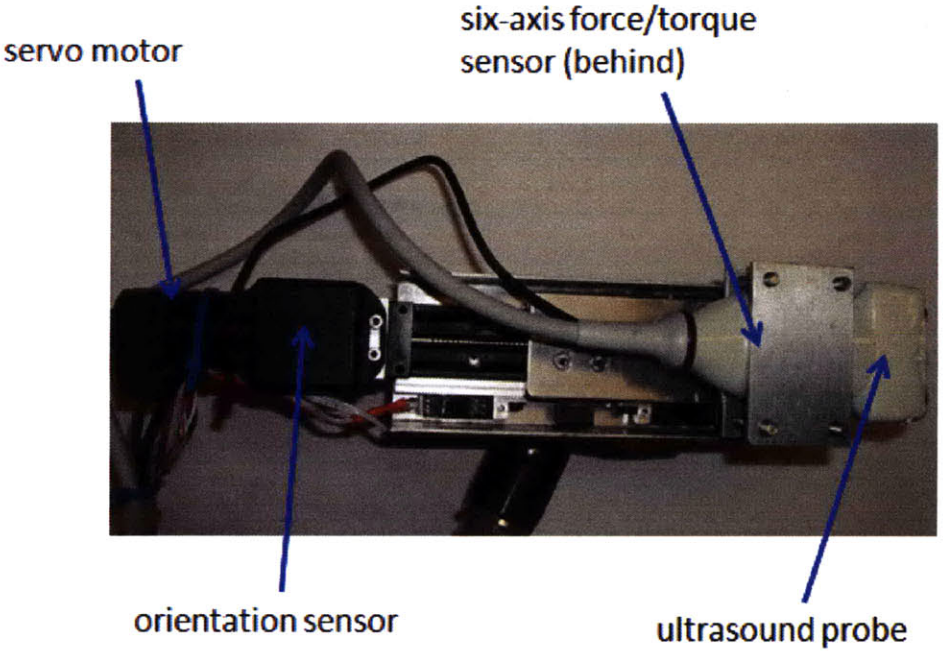
servo motor
six-axis force/torque sensor (behind)
orientation sensor
ultrasound probe

Figure 5-3 The force-controlled ultrasound probe

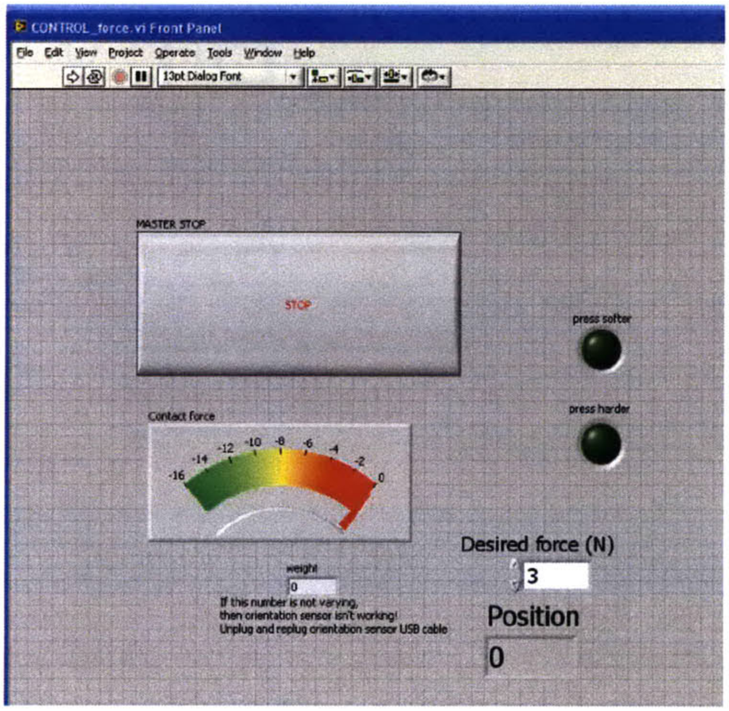
CONTROL_force.vi Front Panel
File Edit View Project Operate Tools Window Help
13pt Dialog Font
MASTER STOP
STOP
press softer
press harder
Contact force
-16
-14
-12
-10
-8
-6
-4
-2
0

weight
0

If this number is not varying,
then orientation sensor isn't working!
Unplug and replug orientation sensor USB cable

Desired force (N)
3

Position
0

Figure 5-4 GUI of the force-controlled probe

5.1.2 Ultrasound Imaging System

The Terason t3000 system was used to perform ultrasound linear scanning using a linear probe array (vermon LA 5.0/128-522) with a center frequency of 5 MHz. The pitch of the array is 0.3 mm, and there are a total of 128 elements. The received waveform is sampled at 30 MHz. Under the assumption that the speed of sound is 1540 m/s, the sampling distance is about 26 μm axially and 150 μm laterally. The physical width of the acquired frame is 38.4 mm and the depth is 50 mm. Note that the time-gain compensation (TGC) was set to be constant along the depth to avoid inhomogeneous amplification that could deteriorate template-based displacement estimation. Figure 5-5 shows the GUI of the ultrasound imaging system.

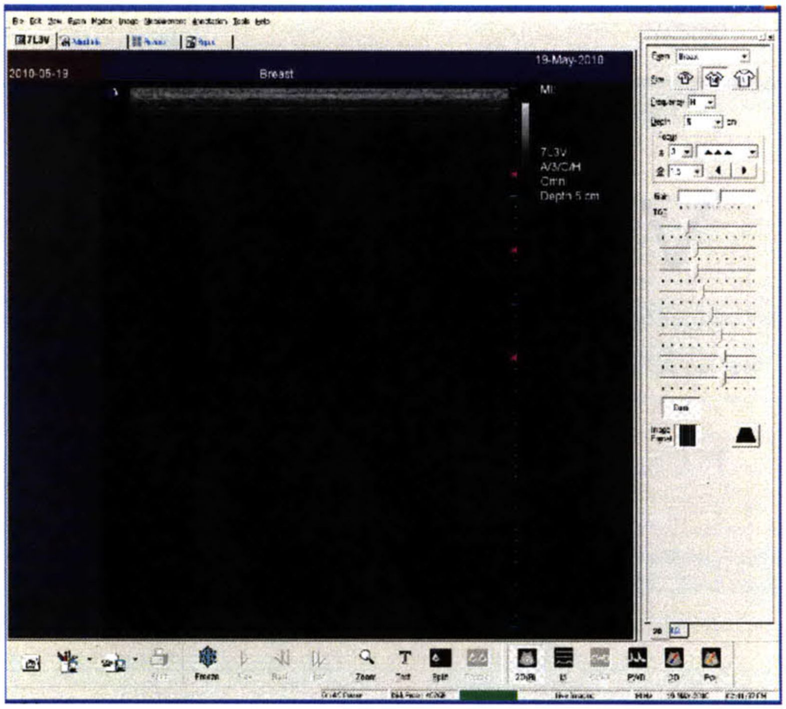

Figure 5-5 GUI of the ultrasound imaging system

It should be emphasized that typically, commercial ultrasound imaging systems provide only post-processed B-mode images. To extract the RF data for displacement estimation, a program was developed in Microsoft Foundation Classes (MFC) by using the streaming RF data software development kit (SDK) provided by Terason. Each acquired frame had 256 scan lines, each of which consisted of 1948 samples. For B-mode image formation, the acquired RF data were demodulated in real time by the Hilbert transform, which was implemented using the algorithm proposed by Marple. [33] The required fast Fourier transform (FFT) operation was implemented using the functions provided in the GNU Scientific Library (GSL). [34]

5.2 Experiment Results and Discussion

In this *in-vitro* experiment, the probe was positioned to scan a particular solid in the breast phantom. The ultrasound images of the solid were acquired under 2.5 N, 3 N, 3.5 N, and 4 N compressions. Displacement estimation was performed on those images using a filtered coarse-to-fine approach, with the parameters summarized in Table 4-2. The deformation correction method was then applied using second-order polynomial curve fitting. The B-mode image under 4 N compression was used to estimate the inclusion appearance under 1 N compression.

Figure 5-6 shows the correction results in the same format as in Section 4.4, and the performance of correction was analyzed in the same procedure. As can be seen in Figure 5-6 (d), the corrected contour agrees with the 1 N-compressed one much better than the uncorrected contour. Those results are quantified and summarized in Table 5-1. After correction, the translational offset between 1 N and 4 N compressions, as measured by the deviation of the centers of area, was reduced by about 80%. Area estimation was also significantly improved.

Similar observations can be made from correcting the 3.5-4 N elastography image to 1 N compression, as shown in Figure 5-7 and Table 5-2. After correction, the translational offset was reduced, and area estimation was significantly improved. However, it can be observed that the inclusion shape in the B-mode image is not very faithfully characterized by that in elastography. This phenomenon could result from the mismatch between the spatial distributions of acoustic impedance and elastic properties, the loss of spatial resolution due to the displacement estimation algorithm, or both.

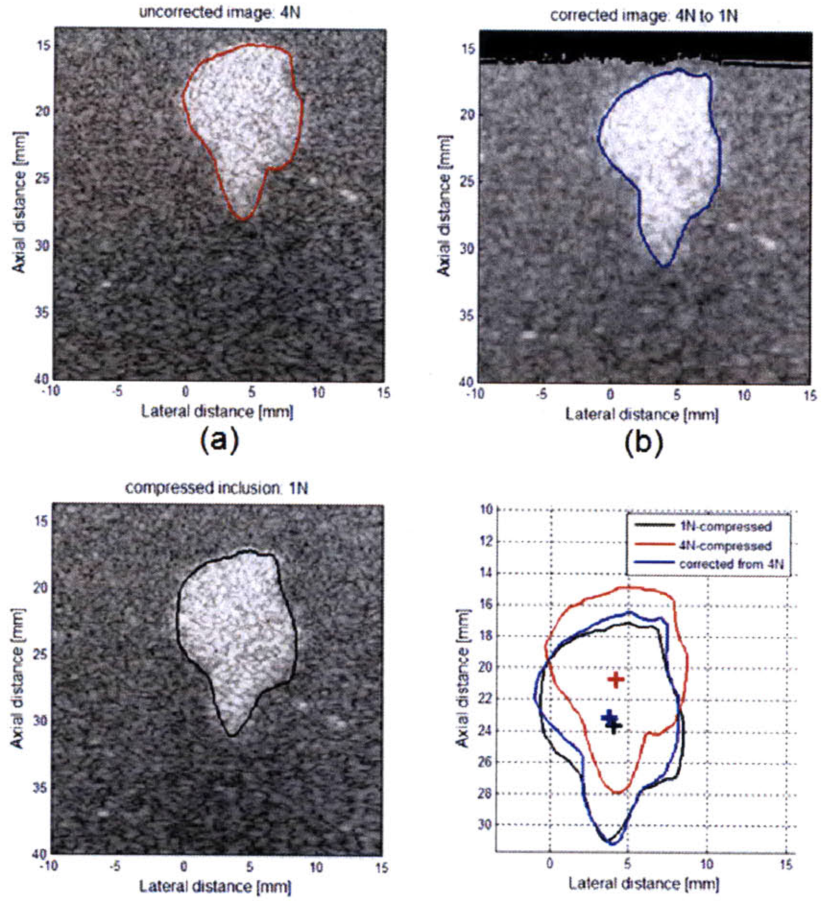
uncorrected image: 4N
corrected image: 4N to 1N
compressed inclusion: 1N
Axial distance [mm]
Lateral distance [mm]
1N-compressed
4N-compressed
corrected from 4N
15
20
25
30
35
40
-10
-5
0
5
10
15

(a) (b)

(c) (d)

Figure 5-6 The B-mode image of the 4 N-compressed inclusion (a) is corrected to 1 N compression (b). From the comparison between (a), (b) and the true 1 N-compressed inclusion contour (c), it is shown that the deviation in the shape and position of the inclusion can be remedied. (d)

Table 5-1 Performance of correcting the 4 N-compressed B-mode image contour to 1 N compression as measured by the translational offset from the true 1 N-compressed contour and the area estimation parameters

	translational offset	**area estimation parameters**		
		TP	**FP**	**FN**
uncorrected	2.99 mm	63.90%	26.75%	36.10%
corrected	0.57 mm	92.85%	6.78%	7.15%

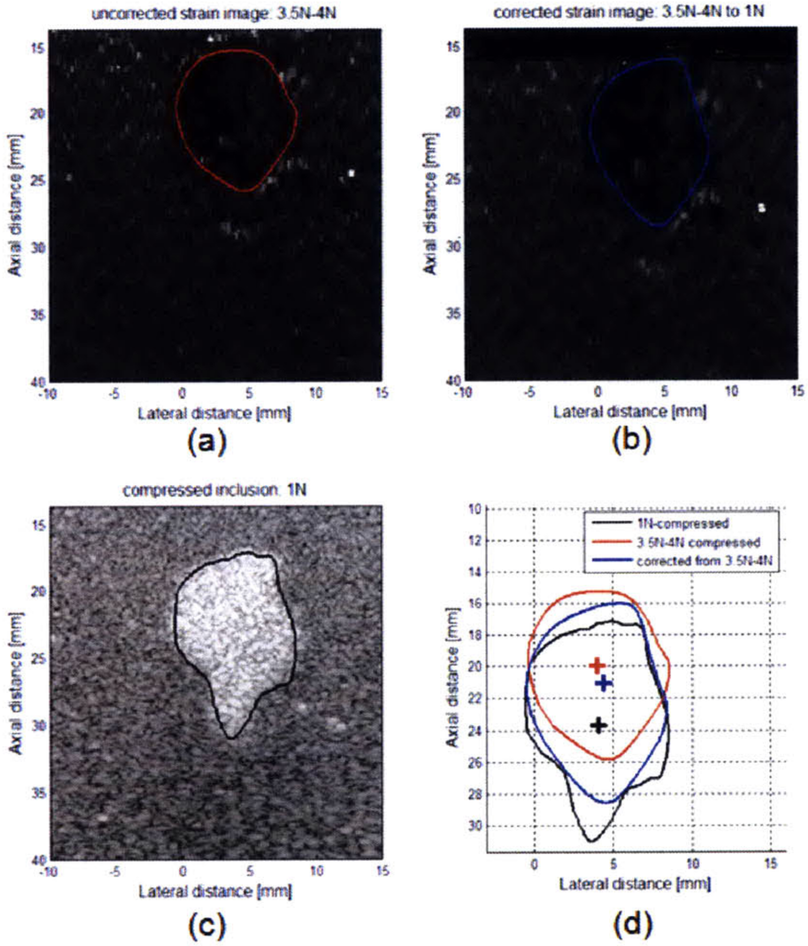
uncorrected strain image: 3.5N-4N
corrected strain image: 3.5N-4N to 1N
compressed inclusion: 1N
Axial distance [mm]
Lateral distance [mm]
15
20
25
30
35
40
-10
-5
0
5
10
15
1N-compressed
3.5N-4N compressed
corrected from 3.5N-4N
10
12
14
16
18
20
22
24
26
28
30
(a)
(b)
(c)
(d)

Figure 5-7 The elastography image under 3.5-4 N compression (a) is corrected to 1 N compression (b). From the comparison between (a), (b) and the true 1 N-compressed inclusion contour (c), it is shown that the deviation in the position of the inclusion can be remedied. (d)

Table 5-2 Performance of correcting the elastography image contour under 3.5-4 N compression to 1 N compression as measured by the translational offset from the true 1 N-compressed B-mode image contour and the area estimation parameters

	translational offset	**area estimation parameters**		
		TP	**FP**	**FN**
uncorrected	3.77 mm	60.97%	21.76%	39.03%
corrected	2.70 mm	85.30%	9.02%	14.70%

5.3 Summary

This chapter presented an *in-vitro* experiment to demonstrate deformation correction on a tissue-mimicking object. A force-controlled ultrasound probe and an ultrasound RF data acquisition system were used to acquire the ultrasound images under specified forces. It was shown that the proposed deformation correction method reduces the translational offset of the object inclusion and improves area estimation in both B-mode imaging and elastography.

Chapter 6

Conclusions

6.1 Summary

In ultrasound imaging, tissue deformation due to probe contact is an inevitable phenomenon and poses challenges for multimodal image registration, 3D reconstruction, and quantitative analysis of the underlying tissue. Most of the existing deformation correction methods rely on assumptions of tissue elastic properties, which are not always measurable in clinical settings. Thanks to the rapid advances of elastography and the related displacement estimation techniques, the reliance on *a priori* knowledge of tissue elasticity for deformation correction could be reduced. In this thesis, a deformation correction method that does not incorporate *a priori* knowledge of tissue elasticity was developed in the framework of elastography.

Similar to elastography, a sequence of ultrasound images is acquired to characterize the mechanical behaviors of the underlying tissue. A force sensor is used to measure the applied force. Through displacement estimation, trajectories of pixels during compression are estimated. Extrapolation or interpolation is then performed on the trajectories to estimate the B-mode or elastography image under a specified contact force.

To optimize the quality of trajectory building and performance of elastography, a correlation-based two-dimensional displacement estimation method incorporating several features was developed. A coarse-to-fine approach was used to utilize the advantages of both using RF data and envelopes for displacement estimation, while reducing the computational cost at the same time. Correlation filtering was incorporated to improve the quality of correlation estimation with reduced loss of spatial resolution. A two-dimensional cosine curve fitting strategy was used to achieve subsample accuracy. Finally, a smoothing scheme with non-uniform spatial resolution was used to reduce noise in the estimation results while reserving high spatial resolution in regions of high quality estimation. The performance of this displacement estimation method was analyzed in a simulation framework incorporating FEM and ultrasound simulation. It was found that the coarse-to-fine search scheme outperformed single-level search and correlation filtering in coarse scale brought noticeable improvement in estimation quality. The tradeoffs in selection of parameters were also examined and discussed.

The performance of polynomial curve fitting, the other important component of the proposed deformation correction method, was also investigated through the simulation framework and noise modeling in force control. The strategies of image acquisition and polynomial order selection were evaluated. Furthermore, it was found that, using polynomial curve fitting, a finer force resolution gave better performance in predicting pixel positions at zero force.

Finally, the proposed deformation correction method was tested through simulation and *in-vitro* experiments. The performance of correction was quantified by translational offset and area estimation of the tissue inclusions. It was found that, for both B-mode and elastography images, those performance metrics were significantly improved after correction. Moreover, it was shown that a finer force resolution gave better performance in deformation correction, which agreed with the analysis of polynomial curve fitting.

6.2 Future Work

To accurately characterize the mechanical behaviors of biological tissue under probe compression, it is important to find a good model for curve fitting. Currently, polynomial functions are employed and promising results are shown, but various kinds of functions, ideally inspired by the theory of solid mechanics, can be tested. Moreover, non-parametric regression models, whose estimates can be updated solely by using the newly acquired data, could be considered when adding samples on the fly is found to be beneficial.

The characterization of the mechanical behaviors is also influenced by the speed of compression. In the FEM simulation here, the compression is assumed to be quasi-static, that is, the inertial effects are ignored. Actually, the speed of compression could potentially affect the displacement-force relationship of biological tissue. This factor should be examined if the speed of compression can be precisely and stably controlled in the experimental setting. Note that the tested speed should still allow stable compression by the practitioner as in elastography. Otherwise, the probe elevational offset in acquiring the sequence of images will cause significant increase in displacement estimation errors due to loss of waveform correlation.

In addition to using a linear array probe as an indenter, the proposed method could also be extended to using convex arrays, which allow a larger field of view. The extension involves modification of the displacement estimation method to allow misalignment of the directions of compression and ultrasound beam propagation.

Reducing the computational cost is also crucial to the practical use of the proposed method. One of the possible means is to implement this method in a parallel computing framework since estimation of the displacement field, the major source of computation, can be divided into a large number of uncorrelated computational tasks. Additionally, prior estimation results may be utilized to significantly speed up the computation. [35]

Finally, the proposed deformation correction method can potentially be extended to reduce random noise in B-mode imaging and elastography. It has been widely shown that random noise in ultrasound images can be reduced by spatial compounding, which combines the images of the same object acquired with different specifications. [36-39] Specifically, Li *et al.* proposed the strain compounding method, which combines images acquired in two different compression levels. [40],[41] The reduction in noise can potentially be enhanced in the framework of the proposed deformation correction method, as the whole sequence of acquired images can be converted into images under a single specified contact force, and the resulting images can then be compounded. In other words, based on the proposed deformation correction technique, it is possible to accomplish the following by one sequence of probe compression:

1. performing elastography
2. deformation correction in B-mode images and elastography
3. noise reduction in B-mode images and elastography

These possibilities will be further explored.

Bibliography

[1] J. Ophir, I. Cespedes, H. Ponnekanti, Y. Yazdi, and X. Li, "Elastography: a quantitative method for imaging the elasticity of biological tissues," *Ultrasonic imaging,* vol. 13, 1991, pp. 111–134.

[2] M.R. Burcher, L. Han, and J.A. Noble, "Deformation Correction in Ultrasound Images Using Contact Force Measurements," *Proceedings of the IEEE Workshop on Mathematical Methods in Biomedical Image Analysis (MMBIA'01),* IEEE Computer Society, 2001, p. 63.

[3] R.M. Comeau, A.F. Sadikot, A. Fenster, and T.M. Peters, "Intraoperative ultrasound for guidance and tissue shift correction in image-guided neurosurgery," *Medical Physics,* vol. 27, 2000, p. 787.

[4] K.D. Paulsen, M.I. Miga, F.E. Kennedy, P.J. Hoopes, A. Hartov, and D.W. Roberts, "A computational model for tracking subsurface tissue deformation during stereotactic neurosurgery," *IEEE Transactions on Biomedical Engineering,* vol. 46, 1999, p. 213.

[5] G.M. Treece, R.W. Prager, A.H. Gee, and L. Berman, "Correction of probe pressure artifacts in freehand 3D ultrasound," *Medical Image Analysis,* vol. 6, 2002, pp. 199–214.

[6] M. Burcher, *A force-based method for correcting deformation in ultrasound images of the breast,* University of Oxford, 2002.

[7] D. Boukerroui, J.A. Noble, and M. Brady, "Velocity estimation in ultrasound images: A block matching approach," *Lecture Notes in Computer Science,* 2003, pp. 586–598.

[8] "Terason t3000 Ultrasound System," http://www.terason.com/products/t3000.asp, August 2010.

[9] E. Konofagou and J. Ophir, "A new elastographic method for estimation and imaging of lateral displacements, lateral strains, corrected axial strains and Poisson's ratios in tissues," *Ultrasound in medicine & biology,* vol. 24, 1998, pp. 1183–1199.

[10] J. Revell, M. Mirmehdi, and D. McNally, "Computer vision elastography: speckle adaptive motion estimation for elastography using ultrasound sequences," *IEEE*

transactions on medical imaging, vol. 24, 2005, p. 755.

[11] X. Chen, M.J. Zohdy, S.Y. Emelianov, and M. O'Donnell, "Lateral speckle tracking using synthetic lateral phase," *IEEE Transactions on Ultrasonics, Ferroelectrics and Frequency Control*, vol. 51, 2004, pp. 540–550.

[12] M. O'Donnell, A.R. Skovoroda, B.M. Shapo, and S.Y. Emelianov, "Internal displacement and strain imaging using ultrasonic speckle tracking," *IEEE Transactions on Ultrasonics, Ferroelectrics and Frequency Control*, vol. 41, 1994, pp. 314–325.

[13] L. Chen, R.J. Housden, G.M. Treece, A.H. Gee, R.W. Prager, and T. Street, "A hybrid displacement estimation method for ultrasonic elasticity imaging," *IEEE Transactions on Ultrasonics, Ferroelectrics, and Frequency Control, in press*, 2010.

[14] R.G. Lopata, M.M. Nillesen, H.H. Hansen, I.H. Gerrits, J.M. Thijssen, and C.L. de Korte, "Performance evaluation of methods for two-dimensional displacement and strain estimation using ultrasound radio frequency data," *Ultrasound in medicine & biology*, vol. 35, 2009, pp. 796–812.

[15] J. Luo and E.E. Konofagou, "Effects of various parameters on lateral displacement estimation in ultrasound elastography," *Ultrasound in medicine & biology*, vol. 35, 2009, pp. 1352–1366.

[16] M.A. Lubinski, S.Y. Emelianov, K.R. Raghavan, A.E. Yagle, A.R. Skovoroda, and M. O'Donnell, "Lateral displacement estimation using tissue incompressibility," *IEEE Transactions on Ultrasonics Ferroelectrics and Frequency Control*, vol. 43, 1996, pp. 247–256.

[17] A.R. Skovoroda, M.A. Lubinski, S.Y. Emelianov, and M. O'Donnell, "Nonlinear estimation of the lateral displacement using tissueincompressibility," *IEEE Transactions on Ultrasonics, Ferroelectrics and Frequency Control*, vol. 45, 1998, pp. 491–503.

[18] G.C. Carter, "Coherence and time delay estimation," *Proceedings of the IEEE*, vol. 75, 1987, pp. 236–255.

[19] R. Zahiri-Azar, O. Goksel, T.S. Yao, E. Dehghan, J. Yan, and S.E. Salcudean, "Methods for the estimation of sub-sample motion of digitized ultrasound echo signals in two dimensions," *Engineering in Medicine and Biology Society, 2008. EMBS 2008. 30th Annual International Conference of the IEEE*, 2008, pp.

5581–5584.

[20] R. Zahiri-Azar and S.E. Salcudean, "P1A-3 Real-Time Estimation of Lateral Displacement Using Time Domain Cross Correlation with Prior Estimates," *IEEE Ultrasonics Symposium, 2006,* 2006, pp. 1209–1212.

[21] M.A. Lubinski, S.Y. Emelianov, and M. O'Donnell, "Speckle tracking methods for ultrasonic elasticity imaging using short-time correlation," *IEEE Transactions on Ultrasonics, Ferroelectrics, and Frequency Control,* vol. 46, 1999, pp. 82–96.

[22] S.W. Huang, J.M. Rubin, H. Xie, R.S. Witte, C. Jia, R. Olafsson, and M. O'Donnell, "Analysis of correlation coefficient filtering in elasticity imaging," *IEEE Transactions on Ultrasonics, Ferroelectrics and Frequency Control,* vol. 55, 2008, pp. 2426–2441.

[23] P.G. De Jong, T. Arts, A.P. Hoeks, and R.S. Reneman, "Determination of tissue motion velocity by correlation interpolation of pulsed ultrasonic echo signals.," *Ultrasonic imaging,* vol. 12, 1990, p. 84.

[24] E. Weinstein and A.J. Weiss, "Fundamental limitations in passive time-delay estimation. II: Wide-band systems," *IEEE transactions on acoustics, speech, and signal processing,* vol. 32, 1984, pp. 1064–1078.

[25] A. Samani and D. Plewes, "A method to measure the hyperelastic parameters of ex vivo breast tissue samples," *Physics in Medicine and Biology,* vol. 49, 2004, pp. 4395–4406.

[26] J.A. Jensen and N.B. Svendsen, "Calculation of pressure fields from arbitrarily shaped, apodized, and excited ultrasound transducers," *IEEE Transactions on Ultrasonics, Ferroelectrics and Frequency Control,* vol. 39, 1992, pp. 262–267.

[27] J.A. Jensen, "Field: A program for simulating ultrasound systems," *Medical and Biological Engineering and Computing,* vol. 34, 1996, pp. 351–352.

[28] J.J. O'Hagan and A. Samani, "Measurement of the hyperelastic properties of tissue slices with tumour inclusion," *Physics in medicine and biology,* vol. 53, 2008, p. 7087.

[29] Matthew Gilbertson, *Handheld Force-Controlled Ultrasound Probe,* Massachusetts Institute of Technology, 2010.

[30] "Active Contours, Deformable Models, and Gradient Vector Flow," http://www.iacl.ece.jhu.edu/static/gvf/, August 2010

[31] C. Xu and J.L. Prince, “Snakes, shapes, and gradient vector flow,” *IEEE Transactions on image processing*, vol. 7, 1998, pp. 359–369.

[32] A. Madabhushi and D.N. Metaxas, “Combining low-, high-level and empirical domain knowledge for automated segmentation of ultrasonic breast lesions,” *IEEE transactions on medical imaging*, vol. 22, 2003, p. 155.

[33] L. Marple Jr, “Computing the discrete-time “analytic” signal via FFT,” *IEEE Transactions on Signal Processing*, vol. 47, 1999, pp. 2600–2603.

[34] “GSL - GNU Scientific Library,” http://www.gnu.org/software/gsl/, August 2010

[35] R. Zahiri-Azar and S.E. Salcudean, “Motion estimation in ultrasound images using time domain cross correlation with prior estimates,” *IEEE Transactions on Biomedical Engineering*, vol. 53, 2006, pp. 1990–2000.

[36] S. Huber, M. Wagner, M. Medl, and H. Czembirek, “Real-time spatial compound imaging in breast ultrasound,” *Ultrasound in medicine & biology*, vol. 28, 2002, pp. 155–163.

[37] C. Hansen, N. Hüttebräuker, W. Wilkening, S. Brunke, and H. Ermert, “Full angle spatial compounding for improved replenishment analyses in contrast perfusion imaging: in vitro studies.,” *ieee transactions on ultrasonics, ferroelectrics, and frequency control*, vol. 55, 2008, p. 819.

[38] R. Rohling, A. Gee, and L. Berman, “Three-dimensional spatial compounding of ultrasound images,” *Medical Image Analysis*, vol. 1, 1997, pp. 177–193.

[39] R.R. Entrekin, B.A. Porter, H.H. Sillesen, A.D. Wong, and P.L. Cooperberg, “Real-time spatial compound imaging: application to breast, vascular, and musculoskeletal ultrasound,” *Seminars in Ultrasound, CT, and MRI*, 2001, pp. 50–64.

[40] P.C. Li and M.J. Chen, “Strain compounding: a new approach for speckle reduction,” *IEEE transactions on ultrasonics, ferroelectrics, and frequency control*, vol. 49, 2002, pp. 39–46.

[41] P.C. Li and C.L. Wu, “Strain compounding: spatial resolution and performance on human images,” *Ultrasound in medicine & biology*, vol. 27, 2001, pp. 1535–1541.